

SPECIAL COLLECTION: MARTIAN ROCKS AND MINERALS: PERSPECTIVES FROM ROVERS, ORBITERS, AND METEORITES

## Visible to near-infrared MSL/Mastcam multispectral imaging: Initial results from select high-interest science targets within Gale Crater, Mars <sup>♠</sup>

DANIKA F. WELLINGTON<sup>1,\*</sup>, JAMES F. BELL III<sup>1</sup>, JEFFREY R. JOHNSON<sup>2</sup>, KJARTAN M. KINCH<sup>3</sup>,  
MELISSA S. RICE<sup>4</sup>, AUSTIN GODBER<sup>1</sup>, BETHANY L. EHLMANN<sup>5,6</sup>, ABIGAIL A. FRAEMAN<sup>6</sup>,  
CRAIG HARDGROVE<sup>1</sup>, AND THE MSL SCIENCE TEAM

<sup>1</sup>School of Earth and Space Exploration, Arizona State University, Tempe, Arizona 85287, U.S.A.

<sup>2</sup>Applied Physics Laboratory, Johns Hopkins University, Laurel, Maryland 20723, U.S.A.

<sup>3</sup>Niels Bohr Institute, University of Copenhagen, 1350 Copenhagen, Denmark

<sup>4</sup>Geology Department, Western Washington University, Bellingham, Washington 98225, U.S.A.

<sup>5</sup>Division of Geological & Planetary Sciences, California Institute of Technology, Pasadena, California 91125, U.S.A.

<sup>6</sup>Jet Propulsion Laboratory, California Institute of Technology, Pasadena, California 91109, U.S.A.

### ABSTRACT

The Mastcam CCD cameras on the Mars Science Laboratory Curiosity Rover each use an 8-position filter wheel in acquiring up to 1600 × 1200 pixel images. The filter set includes a broadband near-infrared cutoff filter for RGB Bayer imaging on each camera and 12 narrow-band geology filters distributed between the two cameras, spanning the wavelength range 445–1013 nm. This wavelength region includes the relatively broad charge-transfer and crystal-field absorption bands that are most commonly due to the presence of iron-bearing minerals. To identify such spectral features, sequences of images taken with identical pointings through different filters have been calibrated to relative reflectance using pre-flight calibration coefficients and in-flight measurements of an onboard calibration target. Within the first 1000 sols of the mission, Mastcam observed a spectrally diverse set of materials displaying absorption features consistent with the presence of iron-bearing silicate, iron oxide, and iron sulfate minerals. Dust-coated surfaces as well as soils possess a strong positive reflectance slope in the visible, consistent with the presence of nanophase iron oxides, which have long been considered the dominant visible-wavelength pigmenting agent in weathered martian surface materials. Fresh surfaces, such as tailings produced by the drill tool and the interiors of rocks broken by the rover wheels, are grayer in visible wavelengths than their reddish, dust-coated surfaces but possess reflectance spectra that vary considerably between sites. To understand the mineralogical basis of observed Mastcam reflectance spectra, we focus on a subset of the multispectral data set for which additional constraints on the composition of surface materials are available from other rover instruments, with an emphasis on sample sites for which detailed mineralogy is provided by the results of ChemMin X-ray diffraction analyses. We also discuss the results of coordinated observations with the ChemCam instrument, whose passive mode of operation is capable of acquiring reflectance spectra over wavelengths that considerably overlap the range spanned by the Mastcam filter set (Johnson et al. 2016). Materials that show a distinct 430 nm band in ChemCam data also are observed to have a strong near-infrared absorption band in Mastcam spectral data, consistent with the presence of a ferric sulfate mineral. Long-distance Mastcam observations targeted toward the flanks of the Gale crater central mound are in agreement with both ChemCam spectra and orbital results, and in particular exhibit the spectral features of a crystalline hematite layer identified in MRO/CRISM data. Variations observed in Mastcam multi-filter images acquired to date have shown that multispectral observations can discriminate between compositionally different materials within Gale Crater and are in qualitative agreement with mineralogies from measured samples and orbital data.

**Keywords:** Mars, multispectral imaging, Curiosity, Gale Crater

### INTRODUCTION

The Mars Science Laboratory (MSL) Curiosity Rover has been exploring the environment of Gale Crater since its successful landing in August 2012. The scientific payload was selected to investigate the potential for past habitable environments through

a detailed investigation of the layered sedimentary units of the central mound, informally known as Mt. Sharp, and the surrounding plains (Grotzinger et al. 2012). A history of aqueous alteration within the crater is indicated by spectral and geomorphologic evidence identified from orbit (e.g., Anderson and Bell 2010; Milliken et al. 2010; Thomson et al. 2011) and is hypothesized to represent a global transition from clay- to sulfate-dominated alteration mineralogy that took place early in the planet's history (e.g., Bibring et al. 2006; Milliken et al. 2010). Multispectral

\* E-mail: dfwellin@asu.edu

<sup>♠</sup> Open access: Article available to all readers online. Special collection papers can be found at <http://www.minsocam.org/MSA/AmMin/special-collections.html>.

imaging capability on Curiosity is provided by the Mast Camera (Mastcam) instrument suite (Malin et al. 2010, 2016 in review<sup>1</sup>; Bell et al. 2012, 2016 in review<sup>1</sup>), which comprises two 1600 × 1200 pixel Bayer-patterned CCD cameras located ~2 m above the surface on the rover's remote sensing mast, along with an accompanying calibration target mounted on the rover deck. Each camera is equipped with an 8-position filter wheel designed to characterize the visible to near-infrared reflectance spectra of surface materials at up to 12 unique wavelengths from 445–1013 nm, including broadband imaging over Bayer filter red, green, and blue (RGB) wavelengths. This wavelength range includes the positions of numerous absorption features of both primary iron-bearing basaltic minerals as well as certain iron-bearing alteration products (e.g., Hunt et al. 1974; Hunt and Ashley 1979; Burns 1993; Clark et al. 2007).

Multispectral observations supplement information on morphology and stratigraphic relationships provided by broadband RGB stereo Mastcam or single-band engineering stereo camera images, which together provide geologic context for other instruments. The importance of this contextual information cannot be overstated: many of the scientific instruments aboard the rover perform measurements with relatively small spot sizes (APXS, MAHLI, ChemCam) or require material to be transferred internally via the Sample Acquisition, Processing, and Handling (SA/SPaH) subsystem (CheMin, SAM) (Grotzinger et al. 2012). Mastcam multispectral observations can document compositional variability within and across geologic units on a broad scale, including distant targets that are out of range to most other rover instruments, to the extent that such variability is observable by the filter set. In the near field they can serve as reconnaissance to identify spectrally distinct materials for follow-up analyses by other instruments. Operational and data volume constraints limit the number of multispectral survey sequences that can be acquired, however, and therefore the development of imaging strategies that make use of a subset of the full pixel array, or of the full filter set, is an ongoing consideration.

As was the case for similar limited-filter visible to near-infrared multispectral imaging on the prior Mars Pathfinder, Mars Exploration Rover, and Phoenix Lander missions (Bell et al. 2000, 2004a, 2004b; Farrand et al. 2007, 2008, 2016; Blaney et al. 2009), even complete Mastcam 12-point spectra are generally not sufficiently diagnostic to provide unique mineralogical interpretations, at least not without separate supporting information. Fortunately, analyses by other on-board instruments can help to constrain the interpretation of Mastcam spectral features. For this reason, we focus in this paper on a subset of multispectral observations acquired in conjunction with multiple other instruments to better understand the mineralogy underlying the observed spectral characteristics. Of most relevance to the interpretation of Mastcam multispectral data are elemental and mineralogical

analyses by ChemCam (Maurice et al. 2012; Wiens et al. 2012), elemental analyses by the Alpha Particle X-ray Spectrometer (APXS; Gellert et al. 2009), and mineralogical analyses by the CheMin X-ray diffraction (XRD) instrument (Blake et al. 2012). In the case of the ChemCam instrument, Johnson et al. (2015) have shown that ChemCam passive observations (acquired when the LIBS laser is not active) can be used to generate relative reflectance spectra in the 400–840 nm wavelength range. This range overlaps significantly with that of the Mastcam filter set, and hence inter-comparisons between the two data sets can provide an important check on the identification of spectral features within the range of overlap (as well as important cross-calibration information for both instrument investigations). Many of the observations presented herein are also the subject of ChemCam passive observations, and detailed interpretations of those data are presented by Johnson et al. (2016).

Because the most diagnostic information on mineralogy is provided by the CheMin XRD instrument, the set of Mastcam spectra presented here primarily focuses on multispectral observations of soil scoops and drill fines that have also been examined by CheMin. While drilling has been the predominant method of sample acquisition, several scoops of soil were processed early in the mission at the Rocknest location (Blake et al. 2013; Anderson et al. 2015b), uncovering fresh material for multispectral analysis in an aeolian sand ripple. The drill, part of the Powder Acquisition Drill System (PADS) portion of the SA/SPaH subsystem, produces a 1.6 cm diameter hole in the surface of up to approximately 5 cm depth (Anderson et al. 2012). The upper ~1.5 cm of material is not collected by the sampling subsystem but is instead distributed on the surface as a tailings pile. Multispectral image sequences of these drill fines allow Mastcam to observe surfaces largely uncontaminated by reddish, Fe<sup>3+</sup>-bearing dust, which influences the visible to near-infrared spectra of practically all surfaces to a varying degree [including, to a lesser extent, surfaces brushed by the Dust Removal Tool (DRT)]. In addition, drill fines are typically subject to analyses by ChemCam and APXS as well, providing a comparatively comprehensive multiple-instrument data set for these targets.

## BACKGROUND

The Mastcam left (M-34, 34 mm focal length) and right (M-100, 100 mm focal length, thus ~3× better spatial resolution than the M-34) cameras each possess a filter wheel holding eight different optical filters for multispectral imaging. One position on each camera is occupied by a broadband infrared-cutoff filter (“filter zero”) for RGB color imaging, making use of the 2 × 2 unit-cell Bayer pattern bonded directly to the detector to acquire three broadband visible wavelength channels. A second filter slot is taken by a narrow-band, 10<sup>-5</sup> neutral-density-coated filter designed for direct solar imaging. The remaining 12 filter positions are occupied by narrow-band filters selected to characterize the visible to near-infrared reflectance spectra of rock, soil, and other targets in the wavelength range of 445–1013 nm (see Table 1 and Fig. 1 for filter bandpass characteristics). The combination of filters between the two cameras provides 12 unique (differing by more than a few nanometers; Bell et al. 2016 in review<sup>1</sup>) center wavelengths for multispectral analysis, including the three RGB Bayer bands. Owing to the presence of

<sup>1</sup> Malin, M.C., Ravine, M.A., Caplinger, M.A., Ghaemi, F.T., Schaffner, J.A., Maki, J.N., Bell, J.F. III, Cameron, J.F., Dietrich, W.E., Edgett, K.S., and others, The Mars Science Laboratory (MSL) Mast cameras and Descent imager: I. Investigation and instrument descriptions, submitted to *Earth & Space Science*, 2016. Bell, J.F. III, Godber, A., McNair, S., Caplinger, M.A., Maki, J.N., Lemmon, M.T., Van Beek, J., Malin, M.C., Wellington, D., Kinch, K.M., and others, The Mars Science Laboratory Curiosity rover Mast Camera (Mastcam) instruments: Pre-flight and in-flight calibration, validation, and data archiving, submitted to *Earth and Space Science*, 2016.

the Bayer pattern, filters below 850 nm have different throughput between nonequivalent Bayer pixels (Malin et al. 2010; Bell et al. 2012, 2016 in review<sup>1</sup>). When lossy JPEG compression is used for downlink of observations made with these narrow-band filters (which it is for most cases), the flight software produces the full-size image by bilinear interpolation from the Bayer color pixel with a wavelength response closest to that of the filter itself, discarding the other Bayer pixels [see also the Software Interface Specification (SIS) document for the instrument, Malin et al. (2013)]. For filters L2 and R2 the Bayer blue pixels are used, for L1 and R1 the greens, and for L3, L4, and R3 the red pixels, effectively decreasing the spatial resolution at these wavelengths by a factor of about 1.4 (for L1/R1) or 2 (for the other short-wavelength filters). The broadband filters L0 and R0 are demosaicked by the algorithm of Malvar et al. (2004) to produce the individual red, green, and blue color images.

Spectral features in the wavelength range of the camera are predominantly due to the crystal-field and charge-transfer absorptions of iron-bearing minerals (e.g., Burns 1993), while most vibrational features lie beyond the sensitivity range of the cameras' silicon CCD detectors. One exception is a narrow H<sub>2</sub>O vibrational overtone/combination band that, in certain hydrated minerals, coincides approximately with the longest wavelength

Mastcam filter. Detection of this feature has been reported in Mars Exploration Rover (MER) Pancam observations (e.g., Wang et al. 2008; Rice et al. 2010) and its detection in Mastcam spectra is being explored by Rice et al. (2013a, 2013b). Broad electronic absorption bands that have been identified on Mars in this wavelength region are attributed to the presence of iron-bearing silicate, oxide, and sulfate minerals (e.g., Bell 1996, 2008). Ferrous silicates such as iron-bearing pyroxenes and olivines possess an absorption band near 1000 nm, a result of a spin-allowed transition of Fe<sup>2+</sup> in octahedral coordination (e.g., Hunt 1977). Reflectance spectra of pyroxenes vary systematically with composition (e.g., Adams 1974), with the 900–1000 nm absorption band tending to shorter wavelengths with lower calcium content. Ferric minerals generally have several charge-transfer bands in this range, as well as a strong charge-transfer band extending from the ultraviolet into the visible (e.g., Hunt and Ashley 1979). As an example, hematite has a distinct band near 860 nm, a shoulder near 630 nm, and an intense absorption wing extending from the ultraviolet into the visible to about 550 nm, formed from overlapping crystal-field and charge-transfer bands (Morris et al. 1985). Nanophase hematite, an X-ray amorphous material in which the particle size is less than approximately 10 nm, lacks distinct crystal-field bands but still possesses a strong iron-oxygen charge transfer

**TABLE 1.** Mastcam RGB Bayer and geology filters effective center wavelengths ( $\lambda_{\text{eff}}$ ) and half-widths at half maximum (HWHM), listed in order of increasing center wavelength

Mastcam Left (M-34)		Mastcam Right (M-100)	
Filter	$\lambda_{\text{eff}} \pm \text{HWHM}$ (nm)	Filter	$\lambda_{\text{eff}} \pm \text{HWHM}$ (nm)
L2	445 ± 10	R2	447 ± 10
LOB	495 ± 37	ROB	493 ± 38
L1	527 ± 7	R1	527 ± 7
LOG	554 ± 38	ROG	551 ± 39
LOR	640 ± 44	ROR	638 ± 44
L4	676 ± 10		
L3	751 ± 10		
		R3	805 ± 10
L5	867 ± 10		
		R4	908 ± 11
		R5	937 ± 11
L6	1012 ± 21	R6	1013 ± 21

Notes: Filters that are (nearly) equivalent between the two cameras are listed on one line; for these filters, reflectance data as shown in subsequent plots are combined to one value. Adapted from Bell et al. (2012).

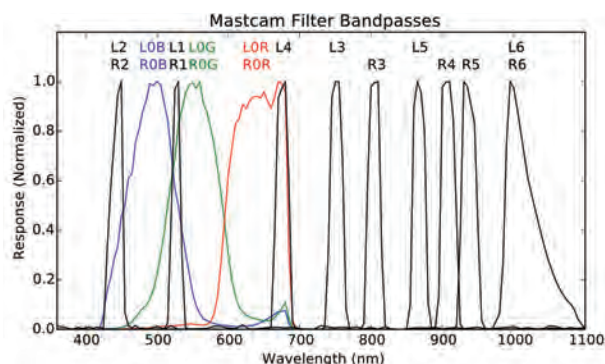


**FIGURE 1.** Mastcam Bayer and narrowband normalized filter profiles for the left and right cameras. The Bayer filter bandpasses (filter 0) are shown in color. For stereo filters, only the left M-34 camera filter profile is plotted, for clarity; the corresponding M-100 profiles are very similar.

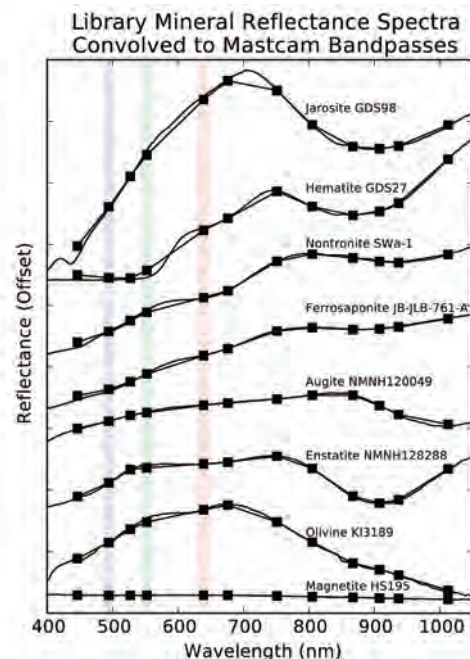


**FIGURE 2.** Mineral spectra from existing spectra libraries are plotted over the Mastcam wavelength range. Reflectance values convolved to Mastcam bandpasses are overlain (points are averaged at overlapping wavelengths). With the exception of magnetite, the spectra are offset vertically for clarity; y-axis tick marks are in intervals of 0.2. See text for discussion of Mastcam reflectance spectra with spectral features similar to those annotated on the plot. The ferrosaponite spectrum is from the RELAB spectral database (acquired by Janice Bishop); the others are drawn from the USGS Digital Spectral Library [splib06a, (Clark et al. 2007)].



absorption edge through the visible wavelengths (Morris et al. 1989). Such nanophase oxides are believed to be primarily responsible for the reddish color of martian dust and soil (Morris et al. 1993, 1997). Representative library spectra of several of these and other iron-bearing minerals that will be mentioned below are shown in Figure 2, along with their values as convolved to the Mastcam filter bandpasses.

Variability in Mastcam spectral data acquired within Gale Crater was anticipated on the basis of orbital observations. Specifically, previous analyses of orbital spectral data have shown evidence for the existence of nontronite, magnesium sulfates, and crystalline hematite in the lowermost layers of Mt. Sharp (Milliken et al. 2010; Thomson et al. 2011). A hematite-rich layer near the base of the mound has been mapped to the uppermost stratum of an erosion-resistant ridge (Fraeman et al. 2013) and should be easily identifiable by Mastcam, whose 867 nm filter is located near the center of a crystalline hematite absorption band. Nontronite possesses features similar to other Fe<sup>3+</sup>-rich minerals, but is distinct from hematite by the longer wavelength position of its broad near-infrared band, centered around 950 nm (e.g., Singer 1982; Bishop et al. 2008). Magnesium sulfates, on the other hand, lack broad absorption features at Mastcam wavelengths (although hydrous varieties possess an H<sub>2</sub>O vibrational band near 1000 nm (e.g., Drake 1995) that may be detectable by the cameras). Iron-bearing varieties of sulfate were not detected from orbit, although this does not preclude the presence of minor or small-scale occurrences that may exist below the detection limit or spatial resolution of orbital instruments. Indeed ferric sulfates have been identified previously at other locations on Mars, both in situ at Meridiani Planum (Christensen et al. 2004; Klingelhöfer et al. 2004) and Gusev Crater (Arvidson et al. 2006; Johnson et al. 2007; Lane et al. 2008) and from orbit at multiple other sites (e.g., Milliken et al. 2008; Bishop et al. 2009; Farrand et al. 2009). Their presence as a minor component of certain bedrock units within Gale Crater has recently been confirmed by the CheMin instrument (Cavanagh et al. 2015; Rampe et al. 2016).

## METHODOLOGY

The conversion of raw Data Number (DN) values of Mastcam multispectral observations to meaningful radiometric quantities involves the use of both pre-flight calibration measurements as well as near-in-time imaging of the onboard Mastcam calibration target during data acquisition (Bell et al. 2006, 2016 in review<sup>1</sup>). The

calibration pipeline is described in detail by Bell et al. (2016 in review<sup>1</sup>), but a brief summary is presented here. Raw observations in the form of Experimental Data Records (EDRs) are decomanded from downlinked 8-bit data back to their original 11-bit dynamic range. For most observations, interpolation over unused Bayer pixels in specific shorter wavelength filters is a step handled by the on-board software, as mentioned in the section above; however, for certain observations in which the full pixel array is returned, this step must be done by the user. In these cases we follow the same debayering method as the flight software. Observations are flat-fielded using normalized relative responsivity arrays derived from sky observations acquired on Curiosity mission sols 36–38. Bias and shutter-smear corrections are not yet implemented but are insignificant components of the measured signal for all but the most extreme observational circumstances (not the case for the observations described here). The average dark current, as measured from masked regions of the detector array, was found to be negligible at the operating temperatures and exposure times of the data reported here, and accordingly these pixel columns are excluded by subframing in most observations. Pixels that possess an 8-bit value of 240 or larger in the raw data are considered saturated on the basis of both pre-flight and in-flight observations, and are ignored as “missing data” in subsequent downstream processing. Flatfielded 11-bit DN values are converted to radiance (W/m<sup>2</sup>/nm/sr) using pre-flight observations of a NIST-calibrated integrating sphere and monochromator measurements of individual filter bandpasses.

To convert from radiance to radiance factor (unitless  $I/F$ , where  $I$  is the measured radiance and  $\pi F$  is the incident solar irradiance), multispectral observations are typically immediately followed or preceded by a sequence of images of the on-board calibration target acquired using the same filter set. In cases where they are not, a calibration target observation from another sol imaged within an hour of the appropriate time of day is used (see Table 2). The Mastcam calibration target is located on the right side of the rover deck approximately 1.2 m from the front windows of the cameras, on top of the Rover Pyro Firing Assembly control box. This calibration target or “caltarget,” which is nearly identical to the Pancam caltarget (Bell et al. 2003, 2006), consists of a ball-and-stick central post (gnomon) surrounded by three grayscale rings and four color chips (Fig. 3). Unlike the MER design, the Mastcam calibration target includes six cylindrical magnets embedded just underneath the surface of the color chips and white and gray rings, which keep the center of the magnet regions comparatively clean while attracting a surrounding ring of magnetic dust (cf., Madsen et al. 2003; Goetz et al. 2008). These “clean spots” provide additional information for assessing the performance of the calibration procedure but are not directly utilized in the calibration pipeline.

Radiance values are extracted from region-of-interest (ROI) selections drawn on the grayscale calibration target rings (avoiding the rings of concentrated dust near the magnet locations). These values are plotted against the laboratory-measured directional-hemispherical reflectance values for the caltarget materials, corrected for illumination and viewing geometry by means of a modified He-Torrance model (He et al. 1991; Bell et al. 2003), and corrected for dust deposition (discussed below). The bidirectional reflectance distribution function model, developed on the basis of prior measurements of the caltarget substrate materials at MER/Pancam wavelengths, was judged to be adequate for Mastcam calibration, which uses parameters determined for a nearby Pancam wavelength to model the directional scattering behavior of the calibration target materials. To determine the coefficient for conversion to radiance factor, we assume that the average ROI radiance values

**TABLE 2.** Observations discussed in the paper along with the calibration target observations used to calibrate each sequence to reflectance

			Observation				Corresponding caltarget		
Sol	SeqID <sup>a</sup>	Target	LTST	Solar elevation	Emission angle	Phase angle	Sol	SeqID <sup>a</sup>	LTST
0084	000372	Rocknest (scoop 2)	14:11	57.0	35.5	66.9	0084	000371	14:09
0084	000373	Rocknest (scoops 3 & 4)	14:14	56.5	30.9	64.1	0084	000371	14:09
0183	000993	John Klein	12:45	66.9	38.8	57.9	0181	000988	12:29
0281	001202	Cumberland	11:10	74.1	41.0	47.6	0281	001201	11:05
0475	001888	Mt. Sharp layers	13:31	55.5	88.0	70.0	0475	001889	13:35
0626	002676	Windjana	12:02	66.1	54.9	69.4	0626	002677	12:07
0721	003084	Perdido	14:13	56.3	31.3	54.3	0721	003085	14:15
0726	003101	Bonanza King	13:39	64.9	34.5	46.6	0725	003097	12:57
0762	003273	Confidence Hills	13:20	69.3	44.6	40.7	0762	003274	13:22
0868	003812	Mojave	12:38	67.5	44.1	45.9	0868	003813	12:40
0883	003851	Mojave (2)	12:06	69.9	41.7	45.5	0883	003852	12:09
0909	003977	Telegraph Peak	11:36	71.7	46.6	62.3	0909	003978	11:39

Notes: Calibration target observations generally immediately precede or follow multispectral sequences, but due to operational or data volume constraints a previously acquired caltarget observation may be considered sufficient. Local true solar time (LTST) and photometric angles are listed for the first observation in the sequence; a single-pointing full-filter multispectral observation may take up to four-and-a-half minutes to run. Photometric angles listed here do not account for local topography, which is especially relevant for the sol 475 multispectral that targets the mound. <sup>a</sup> The SeqID is the 6-digit sequence ID that occurs in product file names following the four-digit sol number and the two-digit instrument identifier.

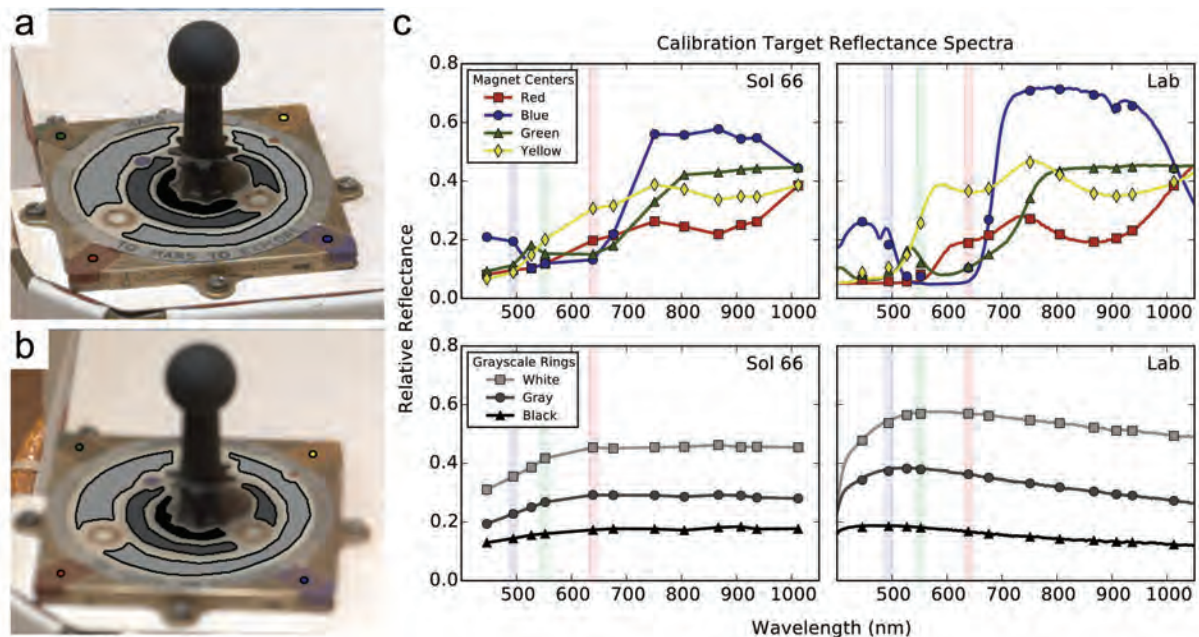


**FIGURE 3.** The Mastcam calibration target as imaged on sol 66 by (a) the left (M-34) and (b) the right (M-100) Mastcam cameras. The M-100 camera cannot focus at the close distance of the calibration target, and therefore ROIs made on right-eye caltarget images carefully avoid edges of caltarget regions within the approximate radius of blur. Rings of magnetic dust surround the location of the six sweep magnets underlying each of the color chips and the white and gray rings. Reflectance calibration makes use of average radiance values extracted from ROIs made on each of the three grayscale rings. Colored regions highlight the source of the data plotted in the accompanying graph. (c) Reflectance spectra from each of the rings and the less dusty color chip magnet region centers, compared with laboratory measured values. Note that lab values are directional-hemispherical reflectances made of the clean substrate material, whereas in-flight data are obtained under different conditions of illumination and with reddish airfall dust as a spectral contaminant. Despite these factors, the sol 66 color chip reflectance curves reproduce the approximate spectral shape of the pigmented substrate materials. The portion of the grayscale rings unaffected by the magnet regions show evidence for a thin layer of deposited dust; caltargets from later sols (not shown) have more substantial dust coatings.

for the three grayscale rings, when plotted against their modeled reflectance values, should fall along a straight line passing through the origin (zero radiance at zero reflectance). The coefficient is derived from the slope of the best-fit line.

A significant complication to this procedure is the deposition of martian dust on the calibration target, even early in the mission owing to material raised during the rover's "sky crane" landing, as well as subsequent gradual deposition of airfall dust from the atmosphere. To account for the influence of the dust on the caltarget reflectance values, a two-layer radiative transfer model (Hapke 1993 section 9.D.3) is employed assuming a uniform layer of dust over the selected caltarget ROIs. The model treats single-scattering events in full detail and uses a two-stream formalism (e.g., Zdunkowski et al. 2007) to treat multiple-scattering events. The dust model and procedure follows very closely the one described in full detail in Kinch et al. (2015), which was developed for dust correction on MER as an improvement to the two-stream model (Kinch et al. 2007) presently implemented for the MER Pancam data sets. The utility of this model for analysis of dusty caltarget surfaces was demonstrated by Johnson et al. (2006) in laboratory studies. Preliminary work on employing the dust model for the MSL Mastcam was presented in Kinch et al. (2013), and the model as employed on Mastcam is described in Bell et al. (2016 in review<sup>1</sup>).

The dust correction procedure fits the scattering model to the three observed caltarget radiances (which are averages of black, gray, and white ring ROI values). The model requires that the dust single-scattering albedo at each wavelength be specified. The spectrum of dust single-scattering albedo values is found from an analysis of all caltarget images over the first 816 sols of the mission. The scattering model, which has two free parameters, is run on all images using many different values for single-scattering albedo. The free parameters are the incoming irradiance and the extinction optical depth of the dust layer on the caltarget. The "correct" albedo value for each filter is the one that results in stable values for the incoming irradiance, given the known variation in Sun-Mars distance and atmospheric dust loading. If the dust was assumed to be too dark, the derived incoming irradi-

ances would drift to higher values as the caltarget gets dustier, and vice versa for dust assumed to be too bright. This procedure as employed on MER Pancam is described in full detail in Kinch et al. (2015). When employed on MSL Mastcam the procedure results in a dust spectrum that is very similar to the spectra derived for the two MERs.

Once the single-scattering albedo spectrum for the dust is determined, the model can be run with those values on every caltarget sequence, returning the best-fit values for the incoming irradiance and dust optical depth. Dusty caltarget reflectance values for each filter can be determined from the model-derived incoming irradiance and radiances. To find the coefficients to convert the images to reflectance, these corrected reflectance values can then be plotted against the measured radiances for the three grayscale rings, and fit with a line passing through the origin, as described above for a clean caltarget.

Observations calibrated to radiance factor ( $I/F$ ) through the above procedure are divided by the cosine of the solar incidence angle to a quantity referred to as "relative reflectance," an approximation of the reflectance factor defined in Hapke section 10.B (1993). Relative reflectance spectra of calibrated observations are presented as the mean values derived from manually defined regions-of-interest (ROIs) made in each camera's field of view and plotted against the filter's effective band-center wavelength. The ROIs from which the values are determined are carefully selected by the following criteria: to include only pixels from a spectrally uniform region, to avoid edges, to be as spatially identical as possible between the two cameras, and to avoid sloping, shadowed, or highly textured regions, to the extent feasible. Saturation sometimes occurs in Mastcam observations, especially in the shortest wavelength filters, as a result of the high contrast between strongly absorbing dust and soil, and less dusty disturbed materials. Pixels within an ROI with saturation in any filter of a multispectral sequence are ignored in others from the same camera to prevent biasing some filter values relative to the others. Right-eye filter values are scaled by the ratio of L6/R6 (these filters are less affected by uncertainties in the dust correction than other, shorter-wavelength stereo filters), to

remove any offset between the two cameras, and averaged with the left-eye values at overlapping wavelengths to produce one merged spectrum. The vertical error bars at each point represent the standard deviation of the selected pixels within each ROI. Note that, therefore, these error bars do not represent the absolute or filter-to-filter uncertainty of the radiometric calibration, but instead represent the variation of the data values within each ROI, which is largely due to small-scale differences in solar incidence angle as a result of the surface texture. Owing to the smaller spatial resolution of the M-34 camera, the standard deviations may be smaller than the M-100 values. The absolute radiometric accuracy for Mastcam has been estimated at 10–20% (Bell et al. 2013). Relative uncertainties are likely similar to values derived for Pancam, for which a filter-to-filter uncertainty of <5% and pixel-to-pixel variation of <1% were reported (Bell et al. 2006).

## RESULTS AND ANALYSIS

Mastcam has acquired hundreds of multispectral observations of science targets along the rover's traverse. In the sections below, we describe in detail the reflectance spectra from the soil scoop marks, drill tailings piles, and a few additional targets for which inferences on specific spectral features can be made on the basis of comparisons with other rover or orbital data sets. A map showing the position of the rover along the traverse path where each included multispectral observation was acquired is shown in Figure 4, while details of the Mastcam observations are listed in Table 2. These spectra are also available as supplemental material<sup>2</sup> published online.

### Rocknest

Curiosity's initial traverse took it in the direction of the "Glenelg" site approximately 450 m to the east of the landing site, where three units identified by orbital mapping adjoin (Anderson

and Bell 2010; Grotzinger et al. 2014). En route, the rover spent several tens of sols (martian days) studying an aeolian deposit at a site called "Rocknest," where five scoops of material were collected and processed by the Collection and Handling for Interior Martian Rock Analysis (CHIMRA) unit to remove any residual contamination and to provide initial sand-sized samples for analysis to the internally housed CheMin and SAM instruments (Blake et al. 2013; Anderson et al. 2015b). The soil scooping operation at Rocknest provided a fresh view of the interior of the sand shadow (Figs. 5a–5c). Multispectral observations were acquired on sol 84 in the M-100 filters only (Fig. 5d), owing to operational constraints. Though CheMin analyses of the basaltic soil revealed >40 wt% mafic silicates (olivines and pyroxenes) as crystalline components (Bish et al. 2013), the reflectance spectra of the sub-surface soils exhibit at best only a weak near-infrared absorption feature. Together with the reddish slope in the visible wavelengths, this result suggests that the reflectance is dominated by an amorphous component with strongly wavelength-varying optical properties in the visible, which may include nanophase and/or poorly crystalline ferric oxides. Indeed, the presence of a substantial iron-bearing amorphous component is supported by mass balance considerations from CheMin and APXS data (Blake et al. 2013). The overall reflectance of the material inside the scoop mark is considerably lower than the dusty surface (Fig. 5a), although some vertical heterogeneity exists in the form of a lighter-toned layer visible in the side wall of each scoop (Figs. 5b–5c), perhaps reflecting dust deposition during a past interlude in sand accumulation. Spectra from neighboring scoop marks in Figure 5 are very similar to each other, with minor differences in reflectance likely attributable to a variation in photometric angles from the relative orientation of walls of the troughs.

### Yellowknife Bay

Curiosity departed the Rocknest location on sol 102 and continued eastward to Glenelg, where it conducted an extensive scientific campaign in and around a topographic depression known as Yellowknife Bay. The strata of the Yellowknife Bay Formation are interpreted to have been deposited in a fluvial-lacustrine setting (Grotzinger et al. 2014), and it is from the stratigraphically lowest member of this formation, the Sheepbed Mudstone unit, that the first two drill samples were obtained on sols 182 and 279, with accompanying Mastcam multispectral observations [for a detailed stratigraphy of this and other Gale Crater units, see Grotzinger et al. (2015)]. The first of these, "John Klein," was preceded by a "mini" drill hole on sol 180, a shallow-depth drilling performed to assess the suitability of the target material for the full-depth drill activity. Figure 6a is a reflectance-calibrated color M-100 RGB image from a multispectral sequence acquired on sol 183 and shows both the mini drill hole (nearer the top of the frame) and full drill hole. Reflectance spectra were derived from an ROI positioned on the mini drill tailings pile, which is distributed more evenly on the surface than the full drill tailings pile. In almost all cases (the one exception being Confidence Hills, as mentioned below), spectra drawn from the tailings of adjacent full and mini

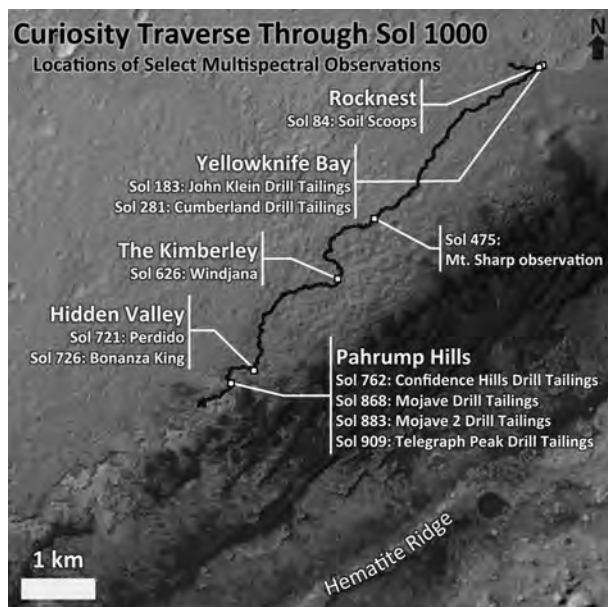


**FIGURE 4.** The MSL/Curiosity rover's traverse path from Bradbury Landing through sol 1000. The rover locations at which each multispectral observation discussed in the text was acquired are marked on the map. Also labeled is a feature referred to as the "Hematite Ridge" that possesses spectral features consistent with crystalline hematite and is visible in long-distance Mastcam observations targeted toward the base of the mound, including the sol 475 multispectral observation. Base map: CTX D22\_035917\_1733\_XN\_06S222W.

<sup>2</sup>Deposit item AM-17-65760, Supplemental Material. Deposit items are free to all readers and found on the MSA web site, via the specific issue's Table of Contents (go to [http://www.minsocam.org/MSA/AmMin/TOC/2017/Jun2017\\_data/Jun2017\\_data.html](http://www.minsocam.org/MSA/AmMin/TOC/2017/Jun2017_data/Jun2017_data.html)).



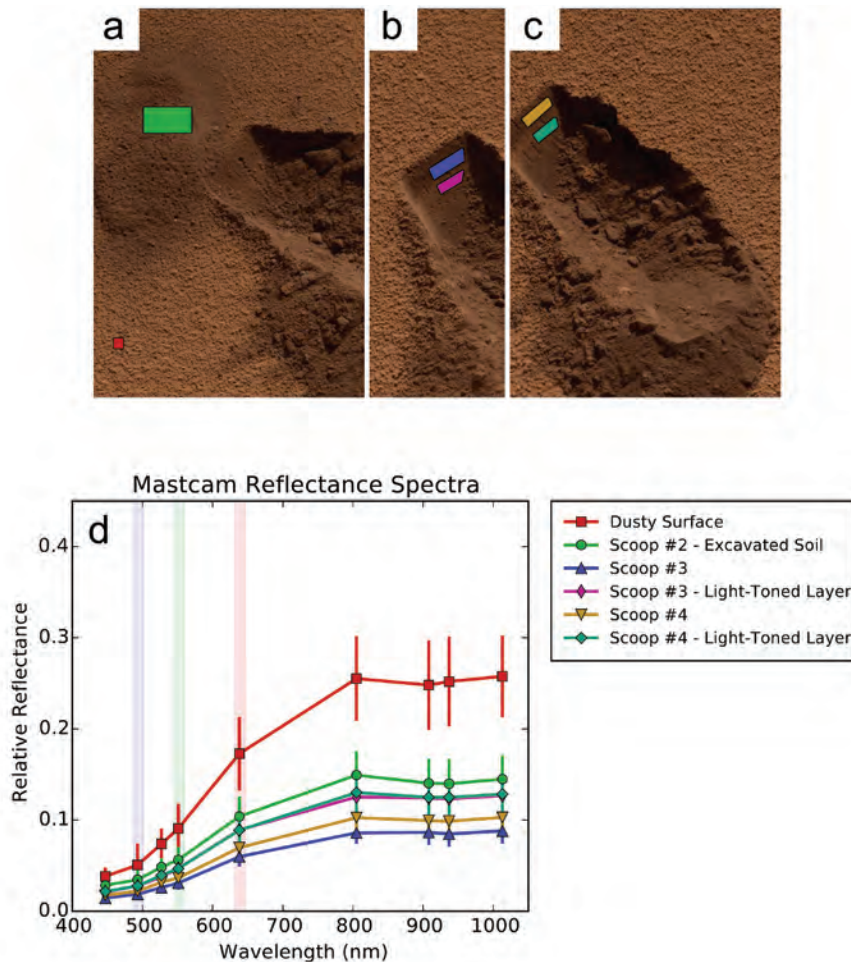


**FIGURE 5.** (a–c) M-100 (R0) reflectance-calibrated color images from sol 84 of soil scoop marks in the Rocknest sand drift, with colored ROIs showing regions whose mean and standard deviation are plotted in **d**. (a) This R0 image shows the second scoop trough made by the rover. ROIs are placed on the excavated soil material and the dusty undisturbed surface (the latter ROI is small, in the lower left of the image). The third (b) and fourth (c) scuffs, both cropped from the same observation, show a lighter-toned layer (lower ROIs) just below darker exposed soil (upper ROIs). For scale, the scuffs are about 4 cm wide. (d) A plot of spectra derived from the pictured ROIs. The two light-toned scoop-layer spectra plot as almost identical. The large standard deviation in the red spectrum values results from small-scale shadows cast on the granular surface, which is illuminated at a relatively low sun angle. Note that there is a difference in solar incidence angles between the material lying on the surface of the aeolian deposit and the material on the walls of the troughs. These spectra are all taken from non-horizontal surfaces and therefore are less comparable, especially in magnitude, to other reflectance values presented in later plots.

drill holes reveal no substantial differences in reflectance. Figure 6b shows the Cumberland full drill hole and tailings pile, located just a few meters from John Klein, and the region of interest from which the mean spectrum was taken. Reflectance spectra for these two sets of drill fines are plotted in Figure 6e, together with spectra derived from other drill targets as well as a dust-covered surface near the John Klein target. Differences between the Sheepbed drill fines and other materials are readily apparent from the plot. Compared to the undisturbed, dusty surface, the Sheepbed drill tailings are substantially less “red” (possess a lesser reflectance slope across the visible wavelength range), as indeed are all of the drill fines. The John Klein and Cumberland tailings possess a clear reflectance maximum near 805 nm, with a broad near-infrared absorption band that appears to be centered shortward of 1000 nm. These VNIR characteristics are consistent with a significant

contribution to the spectral shape from the high abundance of smectite (~20 wt% of total sample) and/or low-Ca pyroxenes (~10 wt%) detected by the CheMin instrument (Vaniman et al. 2014). The library mineral spectra plotted in Figure 2 include a sample of both trioctahedral saponite and Fe<sup>3+</sup>-rich, dioctahedral nontronite, in addition to several other reflectance spectra of mineral species similar to those detected by CheMin in these or subsequent drill samples. The shoulder near 650 nm in the two smectite laboratory spectra does not appear in the multispectral data, suggesting it is either too weak to be apparent at the spectral sampling provided by the filters, or else it is not present (perhaps suppressed by other phases). The ChemCam passive data show an absence of such a band, as well as the beginning of a band in the near-infrared [Fig. 7 and Johnson et al. (2015)], consistent with the multispectral data. It can be seen from the convolved spectra in Figure 2 that

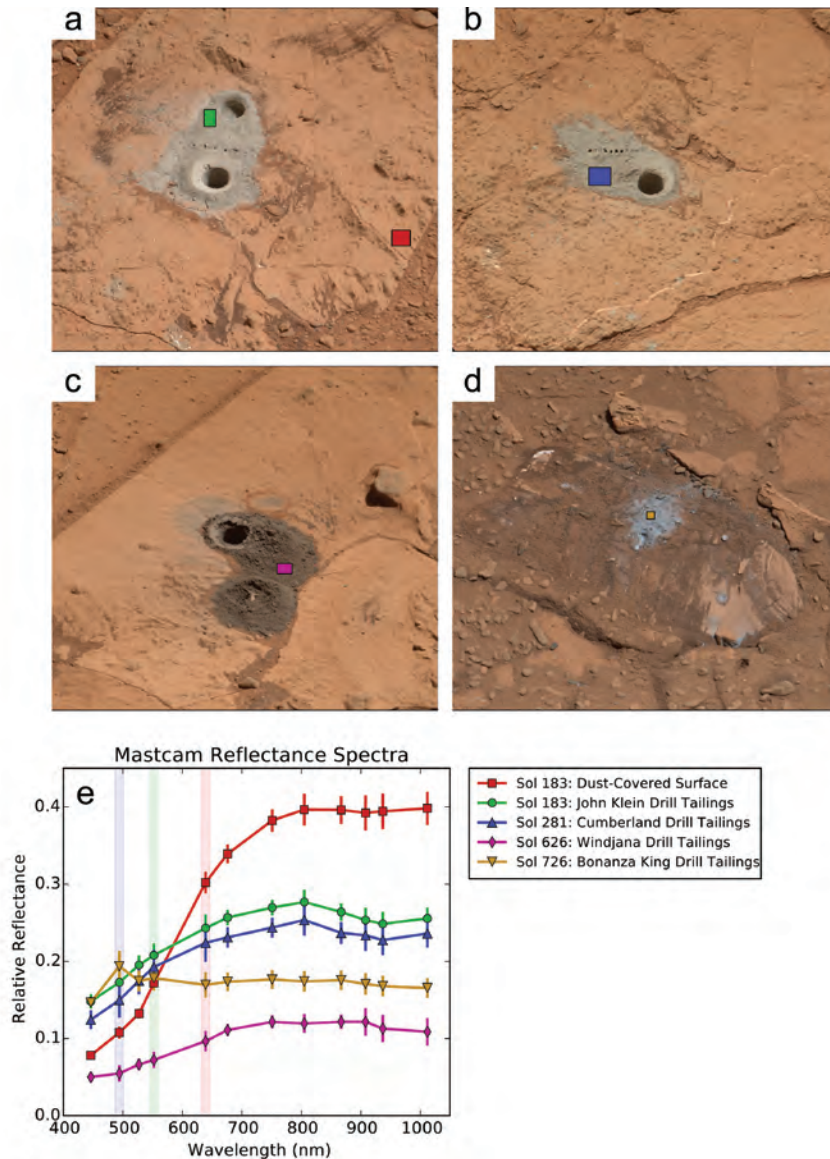


**FIGURE 6.** Drill tailings from Yellowknife Bay (John Klein, sol 183, and Cumberland, sol 281), the Kimberley (Windjana, sol 626), and Hidden Valley (Bonanza King, sol 726) are shown in relative reflectance calibrated M-100 RGB color (a–d), with colored ROIs marking the pixels from which the reflectance spectra values plotted in e are derived. Also shown for comparison with the disturbed materials is the spectrum of a dust-covered surface near the John Klein drill hole. The anomalously high Bayer blue filter in the Bonanza King spectrum may be an artifact introduced by the broad Bayer bandpass. For scale, the drill holes are about 1.6 cm in diameter.

this near-infrared spectral band, which is centered around 950 nm, could be reproduced with either a smectite spectrum or a pyroxene with features intermediate between the augite and enstatite spectra shown. Unlike the library mineral spectra, the Sheepbed material is a complex mixture of multiple mineral and amorphous phases, and the inherently nonlinear nature of such spectral mixtures makes it not straightforward to evaluate quantitatively the relative contribution of each to the overall spectra shape. Compared to the other drill tailings (which do not possess a band at this position), the Sheepbed samples are distinct in possessing significantly more smectite, which may suggest that it is the clay mineral that is contributing substantially to the unique spectral shape.

### The Kimberley

Curiosity did not depart the Yellowknife Bay region until sol 324, and the subsequent emphasis on driving placed nearly 5 km between the Yellowknife Bay drill locations and the next drill hole. The rover arrived at the Kimberley drill location on sol 609 and performed full-depth drilling on sol 621 on a cross-bedded sandstone target in the Dillinger unit (Le Deit et al. 2015; Treiman et al. 2016) named “Windjana,” with an accompanying Mastcam multispectral observation on sol 626. The Windjana drill target produced mini and full drill tailings that are very different from the Sheepbed targets. The observation acquired on sol 626 (Fig. 6c) shows the mini (nearer the bottom



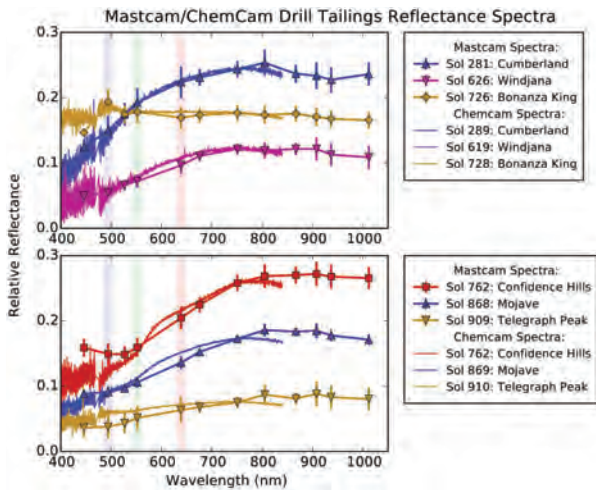


**FIGURE 7.** Mastcam multispectral and ChemCam passive reflectance spectra for six drill tailing targets are shown here for comparison. The top plot includes Mastcam spectra from Figure 6 and ChemCam passive spectra targeting similar drill material; the bottom does likewise for specific Mastcam spectra from Figure 8. The ChemCam data are scaled to the Mastcam filter L3 value in the neighborhood of 751 nm for each spectrum. The spectra pairs in the bottom plot are offset by +0.03, -0.02, and -0.06 (in order of top to bottom) for clarity. ChemCam passive spectra are those from Figure 10 of Johnson et al. (2016); see also Table 1 of that publication for additional details on the ChemCam observations. Note that while the Mastcam ROIs and ChemCam observations target similar material in these observations, they do not have identical spatial coverage; in particular, ChemCam has a very small (0.65 mrad) FOV while the Mastcam spectra are averages over regions shown in preceding figures. The two sets of spectra agree well with each other despite differences in spatial coverage, phase angles, and calibration approach.

of the frame) and full drill holes, the former of which is largely filled in with tailings vibrated back into the hole by the action of the subsequent full drill operation. Spectra derived from the full drill tailings exhibit the lowest overall reflectance of drilled material observed in the mission to date. These low reflectance values are consistent with the relatively higher abundance of strongly absorbing phases, especially higher magnetite (~12 wt% of total sample), reported by the CheMin team (Treiman et al. 2015, 2016). In addition, the reported phyllosilicate abundance in the Windjana drill materials is significantly lower (~10 wt%) than in the Sheepbed drill materials, which may also contribute to the substantially flatter spectral shape near 800 nm as compared to the previous two tailings piles. The general decrease in reflectance at the longest wavelength filters is consistent with absorptions due to mafic minerals.

### Hidden Valley

After the Kimberley, the rover continued driving south and southwest, reaching the boundary of the landing ellipse on sol 672. Near an untraversable patch of sand ripples within a topographic low dubbed “Hidden Valley,” a fourth drill attempt was made on sol 724 on what proved to be an unstable rock slab (“Bonanza King”). Images acquired after the failed mini-drill attempt into the target revealed that the rock had shifted during the drill activity (Anderson et al. 2015a), and thus the decision

was made not to reattempt drilling on this or a nearby rock. Although no XRD data exist for this target, the mini-drill did produce a small pile of fresh tailings suitable for multispectral analysis (Fig. 6d). The resulting spectrum (Fig. 6e) is distinctly different from both the Sheepbed (John Klein and Cumberland) and Windjana spectra. Compared to those previous tailings piles, Bonanza King is intermediate in overall reflectance and extremely flat over the wavelength range sampled by Mastcam filters. (The unreasonably high value for the blue Bayer filter at 494 nm should be considered an artifact, perhaps resulting from the combination of the broad Bayer bandpass with a spectral radiance curve possessing a different shape than that of most other materials observed.) By analogy with other drill tailings spectra, we can make inferences about the mineralogy of Bonanza King despite the lack of X-ray diffraction data from CheMin. The higher overall reflectance as compared to Windjana implies that Bonanza King either has a smaller percentage of the strongly absorbing species such as magnetite that are present in the Windjana sample, or else also possesses a spectrally neutral species with relatively high reflectance, such as a silica phase. From the nearly featureless spectrum of Bonanza King we can also say, qualitatively, that the percentage of other iron-bearing minerals with strong features in these wavelengths, such as hematite, Fe-saponite, and the Fe-sulfate detected nearby (see the discussion of the “Perdido2” target in Johnson et al. (2016) and below), are likely either absent or lower in abundance compared to targets that show these features more clearly. APXS data show that the Mg/Si and Al/Si ratios are quite low for Bonanza King as compared to most other analyses, which may reflect a history of open-system aqueous alteration (Yen et al. 2015). The lack of distinct reflectance features in the multispectral data is broadly consistent with the breakdown of primary mafic minerals as in such a weathering environment.

### Pahrump Hills

After an additional ~600 m of driving, Curiosity began a detailed investigation of basal Mt. Sharp units at Pahrump Hills, where it observed a sequence of predominantly fine-grained mudstones and siltstones that form the lowermost units of the Murray Formation (Stack et al. 2015). Three additional drill samples (“Confidence Hills,” “Mojave 2,” and “Telegraph Peak”) were obtained in these layers on sols 759, 882, and 908 (respectively), with accompanying Mastcam multispectral observations. The first attempt at the Mojave site on sol 867 resulted in only a partial drill hole, which nevertheless produced clean material for multispectral analysis. This target is referred to below as “Mojave,” whereas “Mojave 2” refers to the second, successful drilling that produced a sample for CheMin analysis.

The Confidence Hills drill site was the stratigraphically lowest of the three Pahrump drill locations. Figure 8a shows the mini (lower) and full drill holes and drill tailings. The tailings to the lower left of the drill holes have a slightly higher reflectance (~0.02 higher) than the drill tailings closer to the full drill hole. Unfortunately, the full drill activity significantly disturbed soil from the surrounding surface as well as the tailings pile that previously surrounded the mini drill hole, making it difficult to ascertain the extent to which the tailings piles and soil have been mixed together. The difference in reflectance may be a result of

such mixing. An alternative is that differences in composition and/or grain size exist over spatial scales and/or drill depths as small as that sampled here. Besides this small difference in overall reflectance, the tailings are spectrally similar and show a strong absorption in the shorter wavelength filters (around 550 nm) not present in any of the previous drill tailings spectra (cf. Fig. 6). The CheMin X-ray diffraction data revealed that a significant quantity of crystalline hematite (~8 wt% of total sample; Cavanagh et al. 2015) was present in the sieved sample, compared to <1 wt% in prior samples (Bish et al. 2013; Vaniman et al. 2014; Treiman et al. 2015, 2016). Interestingly, the Mastcam spectra do not show any evidence for a band near 860 nm that is typically associated with fine-grained crystalline hematite (e.g., Morris et al. 1985), nor do they show a downturn beyond about 785 nm as is present in the longest wavelengths of ChemCam passive spectra [Fig. 7 and Johnson et al. (2016)], suggesting that such a band, if present, must be very shallow. The 860 nm band may be largely masked by other constituent minerals. Alternatively, the hematite may be present as a combination of nanophase and crystalline phases, mixtures of which have been shown to vary with respect to the strength of either spectral feature mentioned above (Morris et al. 1989).

Two further full drill holes were acquired in strata of the Pahrump Hills. A mini drill attempt into the original Mojave target resulted in a dislodged block and fines (Fig. 8b). The attempt was repeated successfully a few meters away (Fig. 8c). Spectra from both Mojave targets exhibit essentially identical Mastcam spectra (Fig. 8e). Both spectra have a reddish spectral slope with an inflection near the 527 nm filter consistent with the presence of crystalline hematite, although this feature is weaker than in the Confidence Hills spectrum. By contrast, the Telegraph Peak drill tailings (shown in Fig. 8d) possess a spectrum that is flatter and exhibits little evidence of an absorption near 527 nm. We compute a 527 nm band depth using the relative reflectance values at 446 and 676 nm as  $BD_{527} = 1 - R_{527}/[0.648R_{446} + 0.352R_{676}]$ . The 527 nm band depths for the three Pahrump drill targets are 0.23, 0.13, and 0.04 for Confidence Hills, Mojave 2, and Telegraph Peak, respectively. This parameter correlates well with the measured abundances of crystalline hematite, which were determined by the CheMin team to be ~8, ~4, and ~1 wt%, respectively (Cavanagh et al. 2015; Rampe et al. 2016). Spectral parameters such as these are also influenced by the other constituent minerals; however, within the range of mineralogies sampled by the Pahrump drill holes, such a trend in spectral shape appears to correlate reasonably well with actual hematite abundances.

### Observations of select float rocks and distant mound layers

In addition to the previous spectra of drill powders and scoop marks, several other observations display noteworthy and unique features over the spectral range of the Mastcam filter set and are included to further document the spectral diversity observed by the cameras along first 1000 sols of the rover's traverse. Here we show near-infrared absorption features consistent with iron oxides and iron sulfates in Mastcam spectra, the former in observations targeted at a feature approximately 5 km away that was known from orbital spectral data, and the latter as a

spatially heterogeneous feature observed over generally small (~millimeters) spatial scales at certain locations in rock units explored by the rover near the basal Mt. Sharp stratigraphy. Each of these observations are discussed in turn below, beginning with a feature observed in several small rock fragments in Hidden Valley.

Fresh surfaces of rocks broken by the rover wheels have been very rewarding targets for multispectral observations. One such observation acquired on sol 721 targeted several broken rocks, including the ChemCam target "Perdido" (Fig. 9). Johnson et al. (2016) report numerous detections of a 430 nm band that suggests the presence of a ferric sulfate mineral such as jarosite, particularly when paired with a near-infrared reflectance downturn at wavelengths greater than about 700 nm (e.g., Rossman 1976; Cloutis et al. 2006), with "Perdido2" (a passive ChemCam raster pointed just below the original LIBS Perdido target) expressing this feature most strongly. The 430 nm band is not detectable with Mastcam's filters, but portions of the rock fragment Perdido2 and the surrounding rocks do possess a strong, distinctive absorption in the near-infrared at 900 nm, consistent with a ferric mineral such as jarosite. Unfortunately, the rock fragments are so small (centimeter scale and smaller) that the selection of an appropriate ROI is very difficult in the M-34 images. Figure 9c shows a decorrelation stretch of filters R4, R5, and R6 (908, 937, and 1013 nm), in which bluish colors correspond to material possessing the near-infrared feature. Close examination of the Perdido2 target in this false-color image suggests that the rock may show this feature strongly only on a small portion of its surface. For this reason, the red spectrum in Figure 9d is derived from a nearby fragment expressing this feature in more pixels than the Perdido2 target itself and includes only values from the higher spatial resolution right-camera (M-100) filters. The strongest detection of a 430 nm feature in ChemCam was from the final spot of a  $5 \times 1$  dedicated passive observation (Johnson et al. 2016), whose pointing was extremely close to the portion of the Perdido2 fragment that the decorrelation stretch image suggests may have strong near-infrared Mastcam features as well. A jarosite spectrum from the USGS spectral library (Clark et al. 2007) is shown in Figure 2, depicting the long-wavelength absorption that corresponds favorably with the Mastcam data. While this feature is not uniquely indicative of jarosite, the combination of the Mastcam and ChemCam passive data as well as the subsequent identification of jarosite by CheMin in nearby drill samples (Cavanagh et al. 2015; Rampe et al. 2016) strongly suggests that this ferric sulfate is responsible for this spectral feature.

Long-distance multispectral observations targeting the lower layers of the mound were acquired on sols 468 and 475 (the latter is shown in Fig. 10a), in a coordinated effort with ChemCam passive observations. The field of view included a ridge referred to as the "hematite ridge" from CRISM observations identifying a layer bearing a spectral signature consistent with that oxide (Milliken et al. 2010; Fraeman et al. 2013). Mastcam spectra show that portions of a layer bear a weak but clearly present absorption feature near the 867 nm filter, consistent with crystalline hematite, as well as a weak inflection near 527 nm (Fig. 10c). These observations are consistent with the enhanced 535 band depths and stronger near-infrared downturns observed

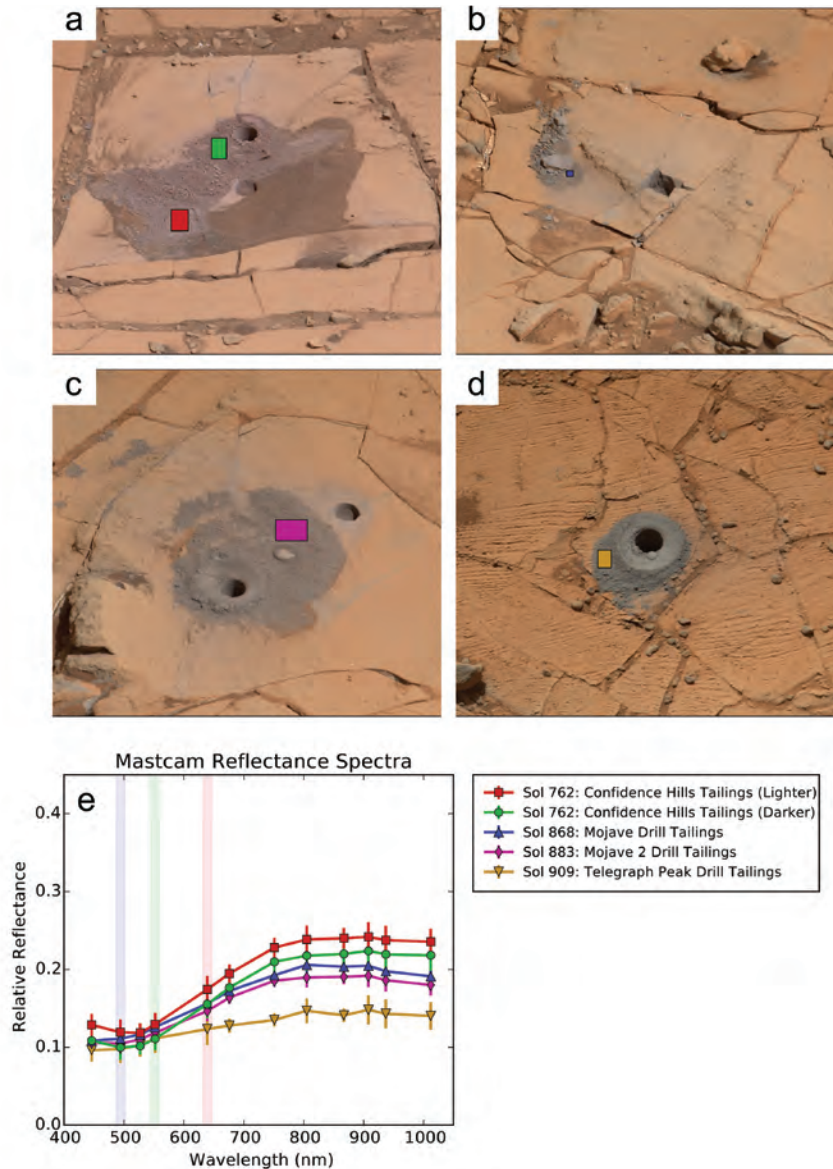


**FIGURE 8.** Drill tailings from the Pahrump Hills drill targets are shown in M-100 RGB color (a–d), with colored ROIs marking the pixels from which the reflectance spectra values plotted in e are derived. Respectively, these drill holes are (a) Confidence Hills (sol 762), (b) Mojave (sol 868), (c) Mojave 2 (sol 883), and (d) Telegraph Peak (sol 909). The Confidence Hills full drill activity disturbed both the reddish soil, which pooled around the drill holes, as well as the drill tailings from a prior “mini” drill hole. Portions of the tailings piles were displaced as a result of the drill vibrations and may have been subject to mixing between themselves and the reddish soil, and so here are labeled only as “lighter” and “darker.” The original target for the second Pahrump drilling, “Mojave,” resulted in a dislodged block (b), but a second attempt (c) was successful.

by ChemCam (Johnson et al. 2016). The presence of the long-wavelength spectral feature as a characteristic of a spatially coherent region of the ridge is most obvious in the decorrelation stretch image of three near-infrared bands shown in Figure 10b, in which the bluish-purple false color corresponds to the region exhibiting this feature. The other layers of the mound visible from this vantage point do not show any distinguishing spectral features. The dunes show a generally low reflectance and broad long-wavelength decrease consistent with a mafic mineralogy, likely with some influence from a thin dust layer. Brighter material appears to lie in a “fan” of material just above the dunes,

but both this material and the topographically higher layers lack any strong or distinctive spectral features aside from the obvious influence of reddish dust at the shorter wavelengths.

### IMPLICATIONS

Mastcam has observed an impressive diversity of reflectance spectra within Gale crater. Tailings from each lithologic unit drilled by the rover have distinctive spectral properties, as do certain small-scale materials observed in broken rock fragments and long distance observations of specific layers of Mt. Sharp. The multispectral data, which track changes in Fe mineralogy, are in good general



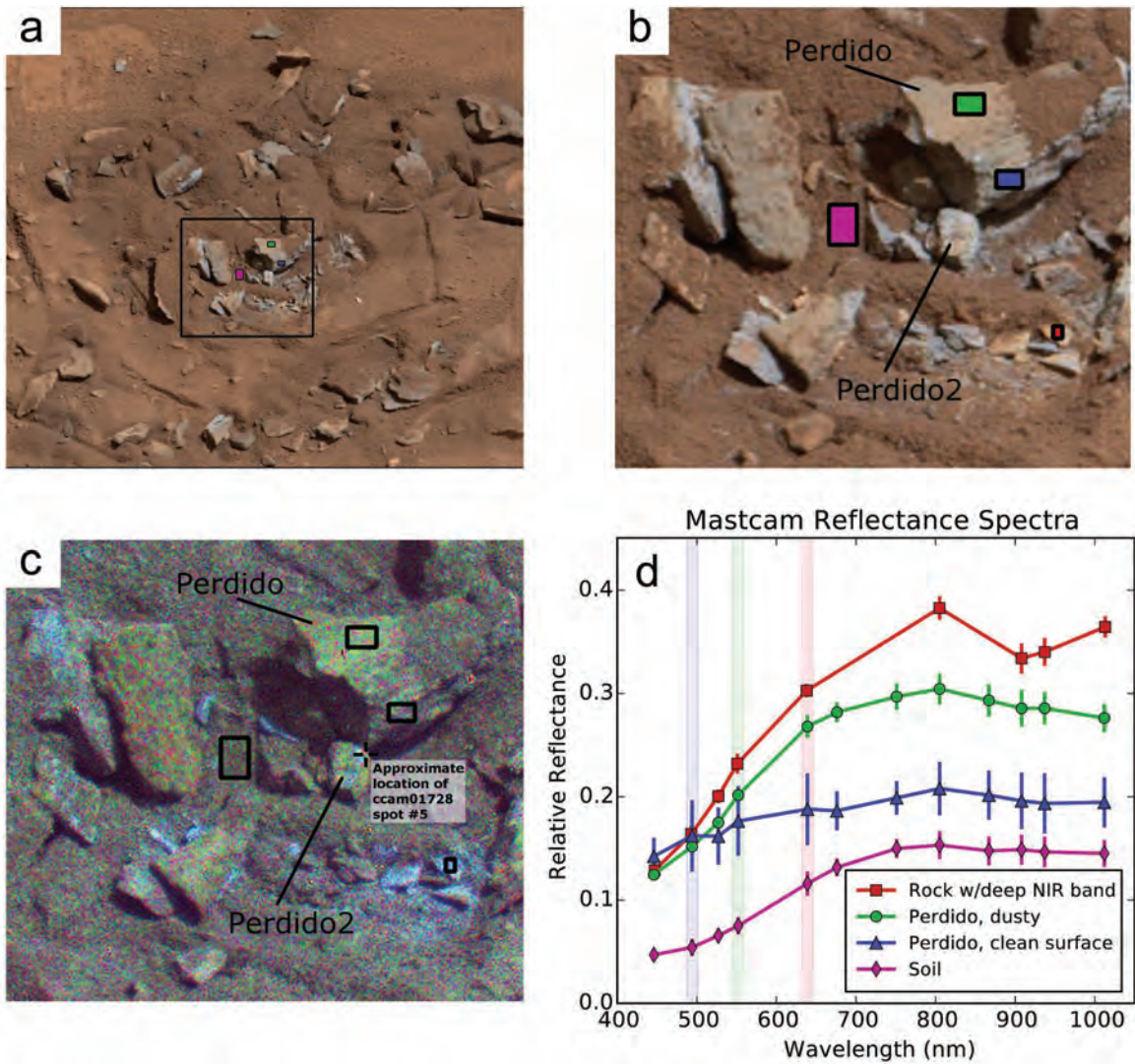


**FIGURE 9.** The M-100 color image (a) from a multispectral observation of the “Perdido” target on sol 721 shows numerous rock fragments broken by the rover wheels. The rocks are float pieces but several clean surfaces are similar to the Bonanza King spectrum, suggesting that they may be sourced from the local bedrock. The black box surrounds a region enlarged in b to show detail. (c) This decorrelation stretch of filters R4, R5, and R6 (908, 937, 1013 nm) shows the small-scale regions with a near-infrared feature (bluish colors). ROIs are shown here as outlines only, to show the underlying DCS colors. It can be seen that small regions of the Perdido2 fragment appear to be consistent with such a feature, although extracting reliable spectra from such a small region is problematic. (d) Spectra from several broken rock fragments, as well as other nearby materials, are shown in the graph. The red ROI covers a region too small to define a corresponding ROI in the M-34; for this reason, only right-eye values are presented. Several of the smaller fragments, including the fragment bearing the red ROI, exhibit spectral features in the near-infrared that may be indicative of a ferric sulfate (see text). The fresh surface of Perdido (blue ROI and spectrum) is spectrally quite flat compared to the dustier top surface and the reddish soil. The spectrum is similar to the nearby Bonanza King drill tailings, although slightly redder, perhaps owing to the surface being slightly less “clean” than the tailings.

agreement with mineralogical and elemental analyses conducted by other instruments on Curiosity’s payload, which corroborate the detection of discrete compositional units. Clear correlations can be drawn between the mineralogy inferred from CheMin X-ray diffraction data and the visible/near-infrared spectral features identified in calibrated Mastcam spectra, further supported by results from geochemical instruments. Mastcam multispectral and ChemCam passive observations provide two independently calibrated measurements of reflectance and display equivalent features within the

wavelength range where they overlap.

The drill tailings observed at Yellowknife Bay possess an 800 nm spectral peak and minimum near 930 nm, apparently deriving from Fe-bearing phyllosilicates and pyroxenes. Saponite can accommodate a range of iron content and redox state (Kodama et al. 1988; Treiman et al. 2014), which should be manifested by changes in the visible/near-infrared reflectance. Further study may permit using Mastcam VNIR data to resolve between the ferrian saponites studied by Treiman et al. (2014)

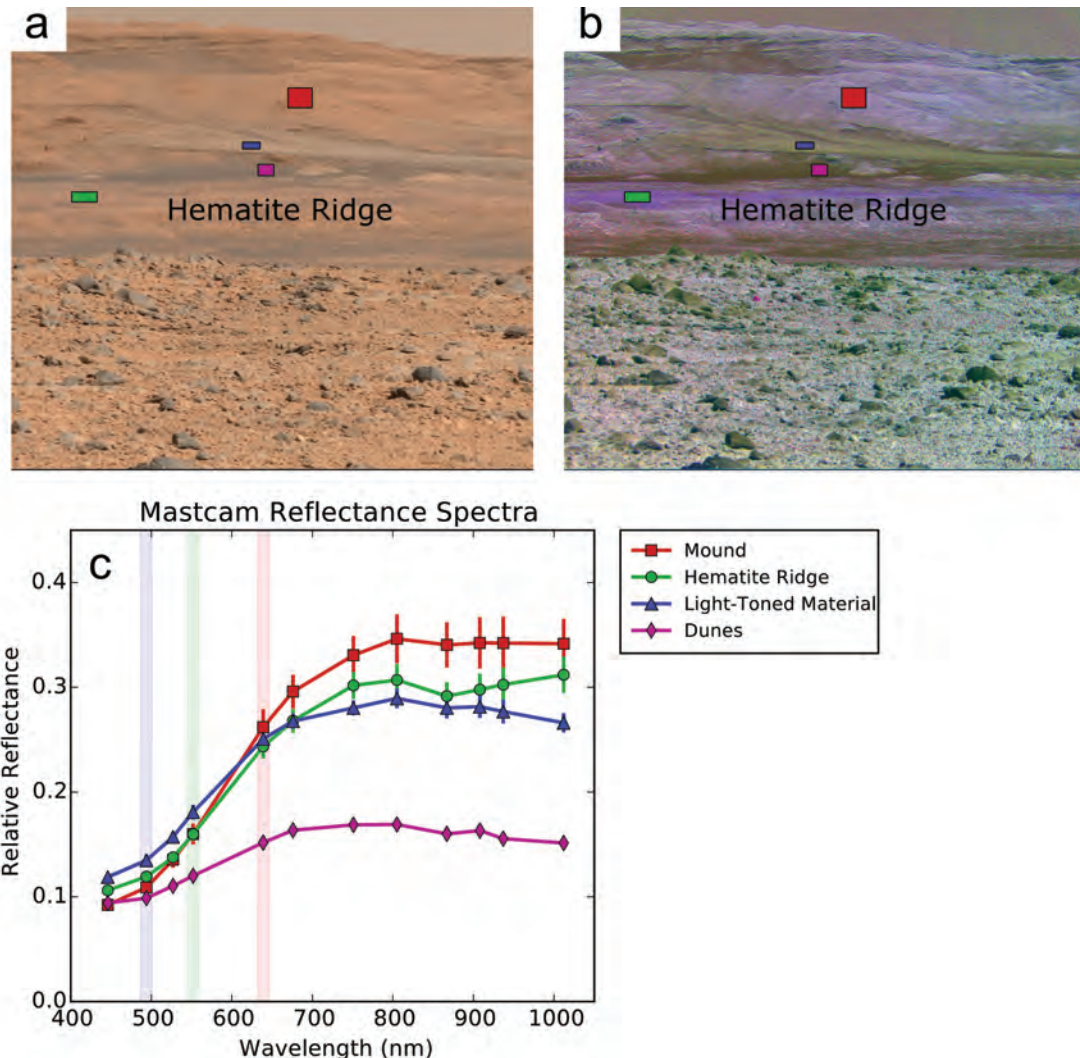


**FIGURE 10.** (a) This M-100 image from sol 475 was aimed toward the layers of the central mound. (b) A false-color decorrelation stretch (using bands at 805, 908, and 1013 nm) demonstrates some of the spectral diversity visible to Mastcam in the lower units of the mound. The spatial extent of the hematite-bearing region associated with the green ROI, which parallels the base of the mound, can be seen in this view. (c) Average Mastcam reflectance spectra of the colored regions. The green spectrum is from the “hematite ridge” and shows features consistent with crystalline hematite. Also shown are spectra of the dunes (purple) and the lighter-toned material (blue) that appears to lie on the sloping surface above the dune field, as well as an average spectrum of the mound (red). This upper mound is spectrally similar to average martian dust, while the other two regions possess a spectral downturn toward longer wavelengths.

and high-Mg ferrosaponites studied by Chemtob et al. (2015) as candidate compositions that fit the 02/ diffraction peak measured by CheMin at Yellowknife Bay.

On the basis of data from other instruments, the identity of other minerals producing distinct spectral features in the Mastcam data set can be reasonably ascertained. The presence of magnetite serves to suppress reflectance across the entire VNIR range, which is most apparent in spectra of the Windjana drill tailings. The Pahrump Hills targets of Confidence Hills and Mojave possess a spectral absorption or inflection near the 527 nm filter consistent with the presence of crystalline hematite and stronger than that in surface dust spectra. The strength of this parameter appears to correlate well with hematite abundances

measured by X-ray diffraction. A longer wavelength hematite feature near the 867 nm filter is not apparent in the drill fines spectra, but does appear weakly in long-distance observations targeted toward the hematite-bearing ridge, whose hematite signature was detected from orbit (Milliken et al. 2010; Fraeman et al. 2013). The ridge, therefore, may possess a greater relative abundance of crystalline hematite than has yet been sampled. A broad 900 nm near-infrared feature observed in Mastcam spectra is consistent with a ferric sulfate mineral, likely jarosite, found in broken rock near the Perdido target, and is correlated with a ~430 nm feature in ChemCam passive data. Detection of the 900 nm feature to date has been limited to material at small spatial scales close to the rover rather than within an extensive



bedrock unit. This limited detection is consistent with the lack of detection in orbital CRISM data as well, which have spatial resolutions of 18 m/pixel. Overall, the Mastcam observations are strongly consistent with the results of ChemCam passive spectra observations on the same targets (Johnson et al. 2016).

Through sol 1000 of the Curiosity mission, the lower mound layers bearing the strongest CRISM signatures of phyllosilicate, sulfate, and iron oxide minerals still lie ahead of the rover. Work by Fraeman et al. (2015) in differentiating CRISM units on the basis of thermophysical and spectral parameters provides a forecast for promising future sites of potential multispectral investigation. Mastcam multispectral observations have demonstrated the ability to identify diversity not readily apparent in RGB color images or orbital spectra. Understanding the mineralogical implications of Mastcam spectral features based on inferences drawn from previous instrument collaborations provides the ability to interpret as well as to distinguish distinct spectral units. The rover's continued ascent up the slopes of Mt. Sharp is expected to bring it into contact with more of the mound's diverse iron mineralogies and associated spectral diversity, including arriving at the hematite ridge itself and the exposures of nontronite expected just beyond (Milliken et al. 2010; Thomson et al. 2011; Fraeman et al. 2013). Further analyses should be able to not only assist reconnaissance spectral imaging for the Curiosity mission, but also provide insight into multispectral analysis of martian materials and imaging strategies relevant for the high-heritage Mastcam-Z instrument (Bell et al. 2014) aboard the upcoming Mars2020 mission, and the similar ExoMars PanCam investigation (Coates et al. 2015) as well.

#### ACKNOWLEDGMENTS

This work was supported by Mars Science Laboratory Project grants and contracts from NASA, JPL/Caltech, and Malin Space Science Systems, Inc. We heartily thank the MSL/Curiosity science and operations team, who made these results possible. The authors also acknowledge specific funding sources, as follows: the MSL Participating Scientist program (J.R. Johnson, JPL contract 1350588, and B.L. Ehlmann), the W.M. Keck Institute for Space Studies and Caltech GPS Division Texaco postdoctoral fellowships (A.A. Fraeman), the NASA Postdoctoral Program (M.S. Rice), and the Danish Council for Independent Research/Natural Sciences (K.M. Kinch, FNU Grant 12-127126). A portion of this research was carried out at the Jet Propulsion Laboratory, California Institute of Technology, under a contract with the National Aeronautics and Space Administration. Finally, the authors thank reviewers Edward Guinness and Jack Mustard for greatly appreciated feedback that allowed us to significantly improve upon the initial manuscript.

#### REFERENCES CITED

- Adams, J.B. (1974) Visible and near-infrared diffuse reflectance spectra of pyroxenes as applied to remote sensing of solid objects in the solar system. *Journal of Geophysical Research*, 79, 4829–4836.
- Anderson, R., and Bell, J.F. III (2010) Geologic mapping and characterization of Gale Crater and implications for its potential as a Mars Science Laboratory landing site. *The Mars Journal*, 5, 76–128.
- Anderson, R.C., Jandura, L., Okon, A.B., Sunshine, D., Roumeliotis, C., Beegle, L.W., Hurowitz, J., Kennedy, B., Limonadi, D., McCloskey, S., and others (2012) Collecting samples in Gale Crater, Mars; an overview of the Mars Science Laboratory Sample Acquisition, Sample Processing and Handling System. *Space Science Reviews*, 170, 57–75.
- Anderson, R.C., Beegle, L., and Abbey, W. (2015a) Drilling on Mars: What we have learned from the Mars Science Laboratory Powder Acquisition Drill System (PADS). The 46th Lunar and Planetary Science Conference, LPI Contribution No. 1832, 2417.
- Anderson, R.C., Beegle, L.W., Hurowitz, J., Hanson, C., Abbey, W., Seybold, C., Limonadi, D., Kuhn, S., Jandura, L., Brown, K., and others (2015b) The Mars Science Laboratory scooping campaign at Rocknest. *Icarus*, 256, 66–77.
- Arvidson, R.E., Squyres, S.W., Anderson, R.C., Bell, J.F., Blaney, D., Brückner, J., Cabrol, N.A., Calvin, W.M., Carr, M.H., Christensen, P.R., and others (2006) Overview of the Spirit Mars Exploration Rover Mission to Gusev Crater: Landing site to Backstay Rock in the Columbia Hills. *Journal of Geophysical Research: Planets*, 111, E02S01.
- Bell, J.F. III (1996) Iron, sulfate, carbonate, and hydrated minerals on Mars. *Geochemical Society Special Publication No. 5*, 359–380.
- Ed. (2008) *The Martian Surface: Composition, Mineralogy and Physical Properties*, 652 p. Cambridge University Press, New York.
- Bell, J.F. III, McSween, H.Y., Crisp, J.A., Morris, R.V., Murchie, S.L., Bridges, N.T., Johnson, J.R., Britt, D.T., Golombek, M.P., Moore, H.J., and others (2000) Mineralogical and compositional properties of Martian soil and dust: Results from Mars Pathfinder. *Journal of Geophysical Research: Planets*, 105, 1721–1755.
- Bell, J.F. III, Squyres, S.W., Herkenhoff, K.E., Maki, J.N., Arneson, H.M., Brown, D., Collins, S.A., Dingizian, A., Elliot, S.T., Hagerott, E.C., and others (2003) Mars Exploration Rover Athena Panoramic Camera (Pancam) investigation. *Journal of Geophysical Research: Planets*, 108, 8063.
- Bell, J.F. III, Squyres, S.W., Arvidson, R.E., Arneson, H.M., Bass, D., Calvin, W., Farrand, W.H., Goetz, W., Golombek, M., Greeley, R., and others (2004a) Pancam multispectral imaging results from the Opportunity rover at Meridiani Planum. *Science*, 306, 1703–1709.
- Bell, J.F. III, Squyres, S.W., Arvidson, R.E., Arneson, H.M., Bass, D., Blaney, D., Cabrol, N., Calvin, W., Farmer, J., Farrand, W.H., and others (2004b) Pancam multispectral imaging results from the Spirit rover at Gusev Crater. *Science*, 305, 800–806.
- Bell, J.F. III, Joseph, J., Sohl-Dickstein, J.N., Arneson, H.M., Johnson, M.J., Lemmon, M.T., and Savransky, D. (2006) In-flight calibration and performance of the Mars Exploration Rover Panoramic Camera (Pancam) instruments. *Journal of Geophysical Research*, 111, E02S03.
- Bell, J.F. III, Malin, M.C., Caplinger, M.A., Ravine, M.A., Godber, A.S., Jungers, M.C., Rice, M.S., and Anderson, R.B. (2012) Mastcam multispectral imaging on the Mars Science Laboratory rover: Wavelength coverage and imaging strategies at the Gale Crater field site. The 43rd Lunar and Planetary Science Conference, LPI Contribution No. 1659, 2541.
- Bell, J.F. III, Godber, A., Rice, M.S., Fraeman, A.A., Ehlmann, B.L., Goetz, W., Hardgrove, C.J., Harker, D.E., Johnson, J.R., Kinch, K.M., and others (2013) Initial multispectral imaging results from the Mars Science Laboratory Mastcam investigation at the Gale Crater field site. The 44th Lunar and Planetary Science Conference, LPI Contribution No. 1719, 1417.
- Bell, J.F. III, Maki, J.N., Mehall, G.L., Ravine, M.A., Caplinger, M.A., and the Mastcam-Z Science Team (2014) Mastcam-Z: A geologic, stereoscopic, and multispectral investigation on the NASA Mars-2020 rover. Presented at the International Workshop on Instrumentation for Planetary Missions (IPM-2014), Greenbelt, Maryland.
- Bibring, J.-P., Langevin, Y., Mustard, J.F., Poulet, F., Arvidson, R., Gendrin, A., Gondet, B., Mangold, N., Pinet, P., Forget, F., and others (2006) Global mineralogical and aqueous Mars history derived from OMEGA/Mars Express data. *Science*, 312, 400–404.
- Bish, D.L., Blake, D.F., Vaniman, D.T., Chipera, S.J., Morris, R.V., Ming, D.W., Treiman, A.H., Sarrazin, P., Morrison, S.M., Downs, R.T., and others (2013) X-ray diffraction results from Mars Science Laboratory: Mineralogy of Rocknest at Gale crater. *Science*, 341, 1238932.
- Bishop, J.L., Lane, M.D., Dyar, M.D., and Brown, A.J. (2008) Reflectance and emission spectroscopy study of four groups of phyllosilicates: smectites, kaolinite-serpentines, chlorites and micas. *Clay Minerals*, 43, 35–54.
- Bishop, J.L., Parente, M., Weitz, C.M., Noe Dobra, E.Z., Roach, L.H., Murchie, S.L., McGuire, P.C., McKeown, N.K., Rossi, C.M., Brown, A.J., and others (2009) Mineralogy of Juventae Chasma: Sulfates in the light-toned mounds, mafic minerals in the bedrock, and hydrated silica and hydroxylated ferric sulfate on the plateau. *Journal of Geophysical Research: Planets*, 114, E00D09.
- Blake, D., Vaniman, D., Achilles, C., Anderson, R., Bish, D., Bristow, T., Chen, C., Chipera, S., Crisp, J., Des Marais, D., and others (2012) Characterization and calibration of the CheMin mineralogical instrument on Mars Science Laboratory. *Space Science Reviews*, 170, 341–399.
- Blake, D.F., Morris, R.V., Kocurek, G., Morrison, S.M., Downs, R.T., Bish, D., Ming, D.W., Edgett, K.S., Rubin, D., Goetz, W., and others (2013) Curiosity at Gale Crater, Mars: Characterization and analysis of the Rocknest sand shadow. *Science*, 341, 1239505.
- Blaney, D.L., Archer, D., Arvidson, R., Cull, S., Ellehöj, M., Fisher, D., Hecht, M., Lemmon, M., Mellon, M., Morris, R.V., and others (2009) Multi-spectral imaging of the Phoenix landing site: Characteristics of surface and subsurface ice, rocks, and soils. The 40th Lunar and Planetary Science Conference, LPI Contribution No. 1468, 2047.
- Burns, R.G. (1993) *Mineralogical Applications of Crystal Field Theory*, 563 p. Cambridge University Press, New York.
- Cavanagh, P.D., Bish, D.L., Blake, D.F., Vaniman, D.T., Morris, R.V., Ming, D.W., Rampe, E.B., Achilles, C.N., Chipera, S.J., Treiman, A.H., and others (2015) Confidence Hills mineralogy and CheMin results from base of Mt. Sharp, Pahrump Hills, Gale Crater, Mars. The 46th Lunar and Planetary Science Conference, LPI Contribution No. 1832, 2735.
- Chemtob, S.M., Nickerson, R.D., Morris, R.V., Agresti, D.G., and Catala, J.G. (2015) Synthesis and structural characterization of ferrous trioctahedral smectites: Implications for clay mineral genesis and detectability on Mars. *Journal of Geophysical*



- Research: Planets, 120, 2014JE004763.
- Christensen, P.R., Wyatt, M.B., Glotch, T.D., Rogers, A.D., Anwar, S., Arvidson, R.E., Bandfield, J.L., Blaney, D.L., Budney, C., Calvin, W.M., and others (2004) Mineralogy at Meridiani Planum from the Mini-TES Experiment on the Opportunity Rover. *Science*, 306, 1733–1739.
- Clark, R.N., Swayze, G.A., Wise, R.A., Livo, K.E., Hoefen, T.M., Kokaly, R.F., and Sutley, S.J. (2007) USGS Digital Spectral Library splib06a. Digital Data Series 231, U.S. Geological Survey.
- Cloutis, E.A., Hawthorne, F.C., Mertzman, S.A., Krenn, K., Craig, M.A., MarciNo, D., Methot, M., Strong, J., Mustard, J.F., Blaney, D.L., and others (2006) Detection and discrimination of sulfate minerals using reflectance spectroscopy. *Icarus*, 184, 121–157.
- Coates, A.J., Jaumann, R., Schmitz, N., Leff, C.E., Josset, J.-L., Griffiths, A.D., Paar, G., Hancock, B., Barnes, D.P., Tyler, L., and others (2015) PanCam on the ExoMars 2018 Rover: A Stereo, Multispectral and High-Resolution Camera System to Investigate the Surface of Mars. The 46th Lunar and Planetary Science Conference, LPI Contribution No. 1832, 1812.
- Drake, N.A. (1995) Reflectance spectra of evaporite minerals (400–2500 nm): applications for remote sensing. *International Journal of Remote Sensing*, 16, 2555–2571.
- Farrand, W.H., Bell, J.F., Johnson, J.R., Jolliffe, B.L., Knoll, A.H., McLennan, S.M., Squyres, S.W., Calvin, W.M., Grotzinger, J.P., Morris, R.V., and others (2007) Visible and near-infrared multispectral analysis of rocks at Meridiani Planum, Mars, by the Mars Exploration Rover Opportunity. *Journal of Geophysical Research: Planets*, 112, E06S02.
- Farrand, W.H., Bell, J.F., Johnson, J.R., Arvidson, R.E., Crumpler, L.S., Hurowitz, J.A., and Schröder, C. (2008) Rock spectral classes observed by the Spirit Rover's Pancam on the Gusev Crater Plains and in the Columbia Hills. *Journal of Geophysical Research: Planets*, 113, E12S38.
- Farrand, W.H., Glotch, T.D., Rice, J.W. Jr., Hurowitz, J.A., and Swayze, G.A. (2009) Discovery of jarosite within the Mawrth Vallis region of Mars: Implications for the geologic history of the region. *Icarus*, 204, 478–488.
- Farrand, W.H., Johnson, J.R., Rice, M.S., Wang, A., and Bell, J.F. (2016) VNIR Multispectral Observations of Aqueous Alteration Materials by the Pancams on the Spirit and Opportunity Mars Exploration Rovers. *American Mineralogist*, 101, 2005–2019.
- Fraeman, A.A., Arvidson, R.E., CatalaNo, J.G., Grotzinger, J.P., Morris, R.V., Murchie, S.L., Stack, K.M., Humm, D.C., McGovern, J.A., Seelos, F.P., and others (2013) A hematite-bearing layer in Gale Crater, Mars: Mapping and implications for past aqueous conditions. *Geology*, 41, 1103–1106.
- Fraeman, A.A., Edwards, C.S., Ehlmann, B.L., Arvidson, R.E., Johnson, J.R., and Rice, M.S. (2015) Exploring Curiosity's future path from orbit: The view of lower Mt. Sharp from integrated CRISM, HiRISE, and THEMIS datasets. The 46th Lunar and Planetary Science Conference, LPI Contribution No. 1832, 2124.
- Gellert, R., Campbell, J.L., King, P.L., Leshin, L.A., Lugmair, G.W., Spray, J.G., Squyres, S.W., and Yen, A.S. (2009) The Alpha-Particle-X-Ray-Spectrometer (APXS) for the Mars Science Laboratory (MSL) rover mission. The 40th Lunar and Planetary Science Conference, LPI Contribution No. 1468, 2364.
- Goetz, W., Leer, K., Gunnlaugsson, H.P., Bartlett, P., Basso, B., Bell, J., Bertelsen, P., Binau, C.S., Chu, P.C., Gorevan, S., and others (2008) Search for magnetic minerals in Martian rocks: Overview of the Rock Abrasion Tool (RAT) magnet investigation on Spirit and Opportunity. *Journal of Geophysical Research: Planets*, 113, E05S90.
- Grotzinger, J.P., Crisp, J., Vasavada, A.R., Anderson, R.C., Baker, C.J., Barry, R., Blake, D.F., Conrad, P., Edgett, K.S., Ferdowski, B., and others (2012) Mars Science Laboratory mission and science investigation. *Space Science Reviews*, 170, 5–56.
- Grotzinger, J.P., Sumner, D.Y., Kah, L.C., Stack, K., Gupta, S., Edgar, L., Rubin, D., Lewis, K., Schieber, J., Mangold, N., and others (2014) A habitable fluvio-lacustrine environment at Yellowknife Bay, Gale Crater, Mars. *Science*, 343, 1242777.
- Grotzinger, J.P., Gupta, S., Malin, M.C., Rubin, D.M., Schieber, J., Siebach, K., Sumner, D.Y., Stack, K.M., Vasavada, A.R., Arvidson, R.E., and others (2015) Deposition, exhumation, and paleoclimate of an ancient lake deposit, Gale crater, Mars. *Science*, 350, aac7575.
- Hapke, B. (1993) *Theory of Reflectance and Emittance Spectroscopy*, 469 p. Cambridge University Press.
- He, X.D., Torrance, K.E., Sillion, F.X., and Greenberg, D.P. (1991) A comprehensive physical model for light reflection. *Proceedings of the 18th Annual Conference on Computer Graphics and Interactive Techniques*, 175–186.
- Hunt, G. (1977) Spectral signatures of particulate minerals in the visible and near infrared. *Geophysics*, 42, 501–513.
- Hunt, G.R., and Ashley, R.P. (1979) Spectra of altered rocks in the visible and near infrared. *Economic Geology*, 74, 1613–1629.
- Hunt, G.R., Salisbury, J.W., and Lenhoff, C.J. (1974) Visible and near infrared spectra of minerals and rocks: IX. Basic and ultrabasic igneous rocks. *Modern Geology*, 5, 15–22.
- Johnson, J.R., Sohl-Dickstein, J., Grundy, W.M., Arvidson, R.E., Bell, J.F. III, Christensen, P., Graff, T., Guinness, E.A., Kinch, K., Morris, R., and others (2006) Radiative transfer modeling of dust-coated Pancam calibration target materials: Laboratory visible/near-infrared spectrogoniometry. *Journal of Geophysical Research*, 111.
- Johnson, J.R., Bell, J.F., Cloutis, E., Staid, M., Farrand, W.H., McCoy, T., Rice, M., Wang, A., and Yen, A. (2007) Mineralogical constraints on sulfur-rich soils from Pancam spectra at Gusev crater, Mars. *Geophysical Research Letters*, 34, L13202.
- Johnson, J.R., Bell, J.F. III, Bender, S., Blaney, D., Cloutis, E., DeFlores, L., Ehlmann, B., Gasnault, O., Gondet, B., Kinch, K., and others (2015) ChemCam passive reflectance spectroscopy of surface materials at the Curiosity landing site, Mars. *Icarus*, 249, 74–92.
- Johnson, J.R., Bell, J.F., Bender, S., Blaney, D., Cloutis, E., Ehlmann, B., Fraeman, A., Gasnault, O., Kinch, K., Mouélic, S.L., and others (2016) Constraints on iron sulfate and iron oxide mineralogy from ChemCam visible/near-infrared reflectance spectroscopy of Mt. Sharp basal units, Gale Crater, Mars. *American Mineralogist*, 101, 1501–1514.
- Kinch, K.M., Sohl-Dickstein, J., Bell, J.F. III, Johnson, J.R., Goetz, W., and Landis, G.A. (2007) Dust deposition on the Mars Exploration Rover Panoramic Camera (Pancam) calibration targets. *Journal of Geophysical Research*, 112.
- Kinch, K.M., Madsen, M.B., Bell, J.F., Johnson, J.R., Goetz, W., and MSL Science Team. (2013) Dust on the Curiosity Mast Camera Calibration Target. The 44th Lunar and Planetary Science Conference, LPI Contribution No. 1719, 1061.
- Kinch, K.M., Bell, J.F. III, Goetz, W., Johnson, J.R., Joseph, J., Madsen, M.B., and Sohl-Dickstein, J. (2015) Dust deposition on the decks of the Mars Exploration Rovers: 10 years of dust dynamics on the Panoramic Camera calibration targets. *Earth and Space Science*, 2, 144–172.
- Klingelhöfer, G., Morris, R.V., Bernhardt, B., Schröder, C., Rodionov, D.S., Souza, P.A. de, Yen, A., Gellert, R., Evlanov, E.N., Zubkov, B., and others (2004) Jarosite and hematite at Meridiani Planum from Opportunity's Mössbauer spectrometer. *Science*, 306, 1740–1745.
- Kodama, H., De Kimpe, C.R., and Dejou, J. (1988) Ferrian saponite in a gabbro saponite at Mont Mégantic, Quebec. *Clays and Clay Minerals*, 36, 102–110.
- Lane, M.D., Bishop, J.L., Dyar, M.D., King, P.L., Parente, M., and Hyde, B.C. (2008) Mineralogy of the Paso Robles soils on Mars. *American Mineralogist*, 93, 728–739.
- Le Deit, L., Mangold, N., Forni, O., Blaney, D., Cousin, A., Dromart, G., Fabre, C., Fisk, M., Gasnault, O., Lanza, N., and others (2015) The potassic sedimentary rocks in Gale Crater, Mars as seen by ChemCam onboard Curiosity. The 46th Lunar and Planetary Science Conference, LPI Contribution No. 1832, 1438.
- Madsen, M.B., Bertelsen, P., Goetz, W., Binau, C.S., Olsen, M., Folkmann, F., Gunnlaugsson, H.P., Kinch, K.M., Knudsen, J.M., Merrison, J., and others (2003) Magnetic Properties Experiments on the Mars Exploration Rover mission. *Journal of Geophysical Research: Planets*, 108, 8069.
- Malin, M.C., Caplinger, M.A., Edgett, K.S., Ghaemi, F.T., Ravine, M.A., Schaffner, J.A., Baker, J.M., Bardis, J.D., Dibiase, D.R., Maki, J.N., and others (2010) The Mars Science Laboratory (MSL) Mast-mounted Cameras (Mastcams) flight instruments. The 41st Lunar and Planetary Science Conference, LPI Contribution No. 1533, 1123.
- Malin, M.C., Edgett, K.S., Jensen, E., and Lipkaman, L. (2013) Mars Science Laboratory Project Software Interface Specification (SIS): Mast Camera (Mastcam), Mars Hand Lens Imager (MAHLI), and Mars Descent Imager (MARDI) Experimental Data Record (EDR) and Reduced Data Record (RDR) PDS Data Products. JPL D-75410, ver. 1.2.
- Malvar, H.S., He, L., and Cutler, R. (2004) High-quality linear interpolation for demosaicing of Bayer-patterned color images. In *IEEE International Conference on Acoustics, Speech, and Signal Processing 2004 (ICASSP '04)*, 3, 485–488.
- Maurice, S., Wiens, R.C., Saccoccio, M., Barraclough, B., Gasnault, O., Forni, O., Mangold, N., Baratoux, D., Bender, S., Berger, G., and others (2012) The ChemCam instrument suite on the Mars Science Laboratory (MSL) rover: Science objectives and mast unit description. *Space Science Reviews*, 170, 95–166.
- Milliken, R.E., Swayze, G.A., Arvidson, R.E., Bishop, J.L., Clark, R.N., Ehlmann, B.L., Green, R.O., Grotzinger, J.P., Morris, R.V., Murchie, S.L., and others (2008) Opaline silica in young deposits on Mars. *Geology*, 36, 847–850.
- Milliken, R.E., Grotzinger, J.P., and Thomson, B.J. (2010) Paleoclimate of Mars as captured by the stratigraphic record in Gale Crater. *Geophysical Research Letters*, 37, L04201.
- Morris, R.V., Lauer, H.V., Lawson, C.A., Gibson, E.K., Nace, G.A., and Stewart, C. (1985) Spectral and other physicochemical properties of submicron powders of hematite ( $\alpha$ -Fe<sub>2</sub>O<sub>3</sub>), maghemite ( $\gamma$ -Fe<sub>2</sub>O<sub>3</sub>), magnetite (Fe<sub>3</sub>O<sub>4</sub>), goethite ( $\alpha$ -FeOOH), and lepidocrocite ( $\gamma$ -FeOOH). *Journal of Geophysical Research: Solid Earth*, 90, 3126–3144.
- Morris, R.V., Agresti, D.G., Lauer, H.V., Newcomb, J.A., Shelfer, T.D., and Murali, A.V. (1989) Evidence for pigmentary hematite on Mars based on optical, magnetic, and Mössbauer studies of superparamagnetic (nanocrystalline) hematite. *Journal of Geophysical Research: Solid Earth*, 94, 2760–2778.
- Morris, R.V., Golden, D.C., Bell, J.F. III, Lauer, H.V. Jr., and Adams, J.B. (1993) Pigmenting agents in martian soils: Inferences from spectral, Mössbauer, and magnetic properties of nanophase and other iron oxides in Hawaiian palagonitic soil PN-9. *Geochimica et Cosmochimica Acta*, 57, 4597–4609.
- Morris, R.V., Golden, D.C., and Bell, J.F. III (1997) Low-temperature reflectivity spectra of red hematite and the color of Mars. *Journal of Geophysical Research: Planets*, 102, 9125–9133.
- Rampe, E.B., Ming, D.W., Morris, R.V., Blake, D.F., Bristow, T.F., Chipera, S.J., Vaniman, D.T., Yen, A.S., Grotzinger, J.P., Downs, R.T., and others (2016) Diagenesis in the Murray Formation, Gale Crater, Mars. The 47th Lunar and Planetary Science Conference, LPI Contribution No. 1903, 2543.
- Rice, M.S., Bell, J.F. III, Cloutis, E.A., Wang, A., Ruff, S.W., Craig, M.A., Bailey, D.T., Johnson, J.R., de Souza, P.A. Jr., and Farrand, W.H. (2010) Silica-rich deposits and hydrated minerals at Gusev Crater, Mars: Vis-NIR spectral characterization and

- regional mapping. *Icarus*, 205, 375–395.
- Rice, M.S., Bell, J.F. III, Wellington, D.F., Godber, A., Hardgrove, C.J., Ehlmann, B.L., Grotzinger, J.P., Kinch, K.M., Clegg, S.M., Fraeman, A.A., and others (2013a) Hydrated minerals at Yellowknife Bay, Gale Crater, Mars: Observations from Mastcam's science filters. American Geophysical Union, Fall Meeting 2013, P23C–1795.
- Rice, M.S., Bell, J.F. III, Godber, A., Wellington, D., Fraeman, A.A., Johnson, J.R., Kinch, K.M., Malin, M.C., and Grotzinger, J.P. (2013b) Mastcam multispectral imaging results from the Mars Science Laboratory investigation in Yellowknife Bay. European Planetary Science Congress, 2013, 762.
- Rossman, G.R. (1976) Spectroscopic and magnetic studies of ferric iron hydroxy sulfates: the series  $\text{Fe}(\text{OH})\text{SO}_4 \cdot n\text{H}_2\text{O}$  and the jarosites. *American Mineralogist*, 61, 398–404.
- Singer, R.B. (1982) Spectral evidence for the mineralogy of high-albedo soils and dust on Mars. *Journal of Geophysical Research: Solid Earth*, 87, 10159–10168.
- Stack, K.M., Grotzinger, J.P., Gupta, S., Kah, L.C., Lewis, K.W., McBride, M.J., Miniti, M.E., Rubin, D.M., Schieber, J., Sumner, D.Y., and others (2015) Sedimentology and stratigraphy of the Pahrump Hills outcrop, lower Mount Sharp, Gale Crater, Mars. The 46th Lunar and Planetary Science Conference, LPI Contribution No. 1832.
- Thomson, B.J., Bridges, N.T., Milliken, R., Baldridge, A., Hook, S.J., Crowley, J.K., Marion, G.M., de Souza Filho, C.R., Brown, A.J., and Weitz, C.M. (2011) Constraints on the origin and evolution of the layered mound in Gale Crater, Mars using Mars Reconnaissance Orbiter data. *Icarus*, 214, 413–432.
- Treiman, A.H., Morris, R.V., Agresti, D.G., Graff, T.G., Achilles, C.N., Rampe, E.B., Bristow, T.F., Ming, D.W., Blake, D.F., Vaniman, D.T., and others (2014) Ferrian saponite from the Santa Monica Mountains (California, U.S.A., Earth): Characterization as an analog for clay minerals on Mars with application to Yellowknife Bay in Gale Crater. *American Mineralogist*, 99, 2234–2250.
- Treiman, A.H., Bish, D., Ming, D.W., Grotzinger, J., Vaniman, D.T., Baker, M.B., Chipera, S., Downs, R.T., Morris, R.V., Rampe, E., and others (2015) Mineralogy and genesis of the Windjana sandstone, Kimberley area, Gale Crater Mars. The 46th Lunar and Planetary Science Conference, LPI Contribution No. 1832, 2620.
- Treiman, A.H., Bish, D.L., Vaniman, D.T., Chipera, S.J., Blake, D.F., Ming, D.W., Morris, R.V., Bristow, T.F., Morrison, S.M., Baker, M.B., and others (2016) Mineralogy, provenance, and diagenesis of a potassic basaltic sandstone on Mars: ChemMin X-ray diffraction of the Windjana sample (Kimberley area, Gale Crater). *Journal of Geophysical Research: Planets*, 121, 2015JE004932.
- Vaniman, D.T., Bish, D.L., Ming, D.W., Bristow, T.F., Morris, R.V., Blake, D.F., Chipera, S.J., Morrison, S.M., Treiman, A.H., Rampe, E.B., and others (2014) Mineralogy of a mudstone at Yellowknife Bay, Gale crater, Mars. *Science*, 343, 1243480.
- Wang, A., Bell, J.F. III, Li, R., Johnson, J.R., Farrand, W.H., Cloutis, E.A., Arvidson, R.E., Crumpler, L., Squyres, S.W., McLennan, S.M., and others (2008) Light-toned salty soils and coexisting Si-rich species discovered by the Mars Exploration Rover Spirit in Columbia Hills. *Journal of Geophysical Research: Planets*, 113, E12S40.
- Wiens, R.C., Maurice, S., Barraclough, B., Saccoccio, M., Barkley, W.C., Bell, J.F. III, Bender, S., Bernardin, J., Blaney, D., Blank, J., and others (2012) The ChemCam instrument suite on the Mars Science Laboratory (MSL) rover: Body unit and combined system tests. *Space Science Reviews*, 170, 167–227.
- Yen, A.S., Ming, D.W., Gellert, R., Clark, B.C., Mittlefehldt, D.W., Morris, R.V., Thompson, L.M., and Berger, J. (2015) Silica retention and enrichment in open-system chemical weathering on Mars. The 46th Lunar and Planetary Science Conference, LPI Contribution No. 1832, 2380.
- Zdunkowski, W., Trautmann, T., and Bott, A. (2007) *Radiation in the Atmosphere: A Course in Theoretical Meteorology*, 497 p. Cambridge University Press.

MANUSCRIPT RECEIVED MARCH 1, 2016

MANUSCRIPT ACCEPTED OCTOBER 26, 2016

MANUSCRIPT HANDLED BY BRADLEY JOLLIFF